

# Dust trapping in thin-ringed protoplanetary disks

C.P. Dullemond<sup>1</sup>, T. Birnstiel<sup>2</sup>, N. Troncoso<sup>3</sup>, L. Perez<sup>3</sup>, S. Andrews<sup>4</sup>, A. Isella<sup>5</sup>, J. Huang<sup>4</sup>, Z. Zhu<sup>6</sup>,  
V. Guzmán<sup>7</sup>, M. Benisty<sup>8</sup>, J. Carpenter<sup>9</sup>

(1) Zentrum für Astronomie, Heidelberg University, Albert Ueberle Str. 2, 69120 Heidelberg, Germany

(2) XXXX (3) XXXX (4) XXXX (5) XXXX (6) XXXX

August 13, 2018

**Abstract.** A large fraction of the protoplanetary disks observed with the ALMA Large Programme DSHARP display multiple well-defined and nearly perfectly circular rings in the continuum, in many cases with substantial peak-to-valley contrast. Several of these rings are very narrow in radial extent. In this paper we analyze these results using the assumption that these dust rings are caused by dust trapping in radial pressure bumps. We model this process in a 1-D axisymmetric way, initially with a simple analytic model, then with a more detailed numerical model. We find that ..... **CONCLUSIONS**

**Key words.** accretion, accretion disks – circumstellar matter – stars: formation, pre-main-sequence – infrared: stars

## 1. Introduction

The concept of dust trapping in local pressure maxima has become a central theme in studies of planet formation and protoplanetary disk evolution, because it might provide an elegant solution to several problems in these fields of study. Theories of planet formation are plagued by the “radial drift barrier”: the problem that, as dust aggregates grow by coagulation, they tend to radially drift toward the star before they reach planetsimal size (e.g. Birnstiel et al. 2010). A natural solution to this problem could be the trapping of dust particles in local pressure maxima (Whipple 1972; Kretke & Lin 2007; Barge & Sommeria 1995; Klahr & Henning 1997). Not only does this process prevent excessive radial drift of dust particles, it also tends to concentrate the dust into small volumes and high dust-to-gas ratios, which is beneficial to planet formation. From an observational perspective, the radial drift problem manifests itself by the presence of large grains in the outer regions of protoplanetary disks (Testi et al. 2003; Andrews et al. 2009), which appears to be in conflict with theoretical predictions (Brauer et al. 2007). One possible solution to this observational conundrum could be that the disks are much more massive in the gas than previously suspected, leading to a higher gas friction for millimeter grains and thus longer drift time scales (Powell et al. 2017). Another explanation is to invoke dust traps. The most striking observational evidence for dust trapping seems to come from large transitional disks, which feature giant dust rings, sometimes lopsided, in which large quantities of dust appears to be concen-

trated (Casassus et al. 2013; van der Marel et al. 2013). These observations appear to be well explained by the dust trapping scenario Pinilla et al. (2012a). But these transitional disks seem to be rather violent environments, possibly with strong warps (Marino et al. 2015; Benisty et al. 2017) and companion-induced spirals (Dong et al. 2016). For more “normal” protoplanetary disk the dust traps would have to be more subtle. Pinilla et al. (2012b) explored the possibility that the disk contains many axisymmetric local pressure maxima, and calculated how the dust drift and growth would behave under such conditions. It was found that, if the pressure bumps are strong enough, the dust trapping can keep a sufficient fraction of the dust mass at large distances from the star to explain the observed dust millimeter flux. It would leave, however, a detectable pattern of rings that should be discernable with ALMA observations. Since the multi-ringed disk observation of HL Tau (ALMA Partnership et al. 2015) a number of such multi-ringed disks have been detected (Andrews et al. 2016; Isella et al. 2016; Cieza et al. 2017; Fedele et al. 2017, 2018). It is therefore very tempting to see also these multi-ringed disks as evidence for dust trapping, and as an explanation for the retention of dust in the outer regions of protoplanetary disks.

The data from the ALMA Large Programme DSHARP (**REFERENCES**) offers an exciting new opportunity to put this concept to the test, and to put constraints on the physics of dust trapping in axisymmetric pressure maxima. This is an opportunity which we explore in this paper.

If we assume that the rings seen in our data are caused by dust trapping, the question arises: what constraints do the data impose on the physics of dust trapping? To

Source	$d$ [pc]	$M_*/M_\odot$	$L_*/L_\odot$
AS 209	121	0.832	1.413
Elias 24	136	0.776	6.03
HD 163296	101	2.04	17.0
GW Lup	155	0.457	0.331
HD 143006	165	1.78	3.80

**Table 1.** The stellar parameters assumed for the stars studied in this paper. Distance is in parsec and mass and luminosity are in units of the solar values. More details, as well as references and uncertainty estimates, can be found in Andrews et al. (2018).

explore this we start by studying the rings individually, assuming that the dust does not escape from the ring. This makes it possible to look for a steady-state dust trapping solution in which the radial drift forces (that push the dust to the pressure peak) are balanced by turbulent mixing (that tends to smear out the dust away from the pressure peak). In Section E we will construct a very simplified analytic dust trapping model, and confront this with the most well-isolated rings from our sample. **Describe the next sections.** But before we do the modeling, we review, in Section 2, the key aspects of the data from our ALMA Large Programme that we compare to our models.

## 2. The high-contrast rings of AS 209, Elias 24, HD 163296, GW Lup and HD 143006

In this paper we focus on those sources of the DSHARP Programme that show high-contrast and radially thin rings that are separated by deep valleys, and that are sufficiently face-on to not have to worry much about 3-D line-of-sight issues. These are AS 209, Elias 24, HD 163296, GW Lup and HD 143006. Their stellar parameters are given in Table 1.

A gallery of these sources is shown in Fig. 1. For an overview of the ALMA Large Programme we refer to Andrews et al. (2018), and for an in-depth discussion on the data of the individual sources we refer to Huang et al. (2018), Isella et al. (2018), Guzmán et al. (2018).

The high-contrast rings of these sources provide “clean laboratories” for testing the theory of dust trapping in a ring-by-ring manner. Fig. 2 shows the radial profile (deprojected for inclination) of the thermal emission of the dust of the five disks. The procedure used to extract these radial profiles from the continuum maps is described by Huang et al. (2018), though we removed the blob seen in HD 163296 and HD 143006 for this work.

The brightness profiles are expressed as linear brightness temperature  $I_\nu^{\text{lb}}$ , which we define in Appendix A. The choice of linear brightness temperature over full brightness temperature is important, because the full brightness temperature tends to vastly underestimate the contrast between the rings and the inter-ring regions. The linear brightness temperature is instead linearly proportional to

the intensity in Jy/beam, and thus represents the contrast appropriately.

## 3. Fitting a Gaussian profile to the ring emission

As we will discuss later (Section 6 and Appendix E), for a Gaussian pressure bump the solution to the radial dust mixing and drift problem is, to first approximation, also a Gaussian, with a width smaller than, or equal to, that of the gas pressure bump. Our analysis of the eight rings of this paper therefore naturally starts with the fitting of the observed radial intensity profiles with a Gaussian function. For some [CHECK] of the rings of this paper such Gaussian fits were done in the context of fitting the entire radial intensity profile in the uv-plane to the ALMA data (Guzmán et al.XXXX; More??). Our fits may deviate slightly from those [CHECK], because here we put emphasis on the shape of the peak of the rings, and deemphasize the wings. **CHECK.**

The aim is now to find, for each ring, a Gaussian linear brightness temperature profile

$$I_\nu^{\text{lb,gauss}}(r) = A \exp\left(-\frac{(r - r_0)^2}{2\sigma^2}\right) \quad (1)$$

that best describes the ring. To be more precise: We determine the values of  $A$ ,  $r_0$  and  $\sigma$  for which Eq. (1) best fits the observed linear brightness temperature profile  $I_\nu^{\text{lb,obs}}(r)$  shown in Fig. 2 within a prescribed radial domain as given in Table 2. Details of the fitting procedure are described in Appendix B. The Gaussian fits are shown as inverse parabolas in Fig. 2. In Fig. 3 these Gaussian fits are shown in close-up. The parameters of the best fits are listed in Table 2. For the error estimates on these values, see Appendix B.

The observed rings are the result of the thermal emission of a dust ring convolved with the ALMA beam. To obtain the width of the underlying dust ring we have to deconvolve. Assuming a Gaussian beam and a Gaussian dust ring, we can use the rule of the convolution of two Gaussians, and obtain the width  $w_d$  of the dust ring

$$w_d = \sqrt{\sigma^2 - b^2} \quad (2)$$

where  $b$  is the beam width expressed as standard deviation in units of au. It is computed from  $b_{\text{fwhm,as}}$  (the beam full-width at half-maximum (FWHM) in units of arcseconds) through the equation  $b = d_{\text{pc}} b_{\text{fwhm,as}} / 2.355$ , where  $d_{\text{pc}}$  is the distance to the source in units of parsec. In using Eq. (2) we have ignored the elliptical shape of the beam as well as the inclination of the disk.

The slightly narrower deconvolved ring should also have a correspondingly higher amplitude  $A_{\text{dec}}$  given by

$$A_{\text{dec}} = \frac{\sigma}{w_d} A \quad (3)$$

to conserve luminosity, where we ignore the geometric effects due to the circular coordinates. The values of  $A_{\text{dec}}$  are listed in Table 2 as well.

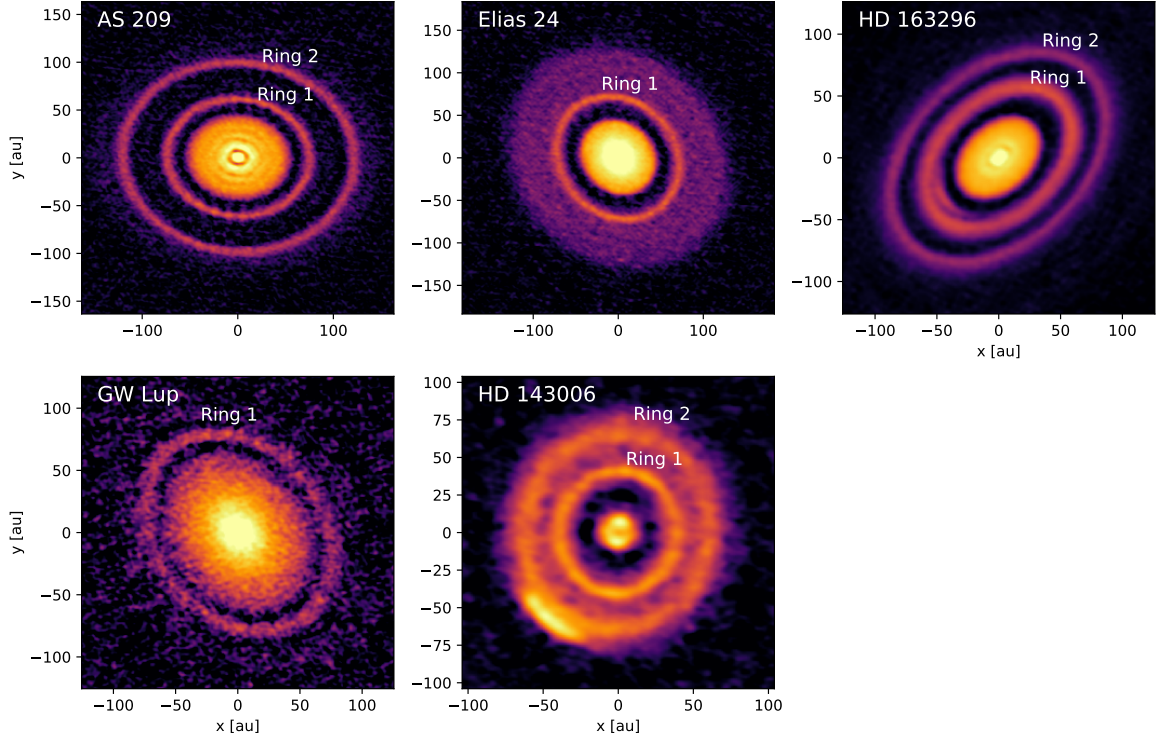


**Fig. 1.** The continuum maps in band 6 of the five disks in our sample which have the most pronounced rings. The eight highest contrast rings, which are the topic of this paper, are marked in the images. For a detailed description of these data, see Guzmán et al. (2018) for AS 209, Isella et al. (2018) for HD 163296, and Huang et al. (2018) for the rest.

For completeness, let us note that the deconvolved Gaussian model then becomes

$$I_{\nu}^{\text{lb,gauss,dec}}(r) = A_{\text{dec}} \exp\left(-\frac{(r-r_0)^2}{2w_d^2}\right) \quad (4)$$

The width of the dust rings in units of the local pressure scale height  $h_p$  (see Table 2) can only be roughly estimated, because we do not know  $h_p$  well enough due to our lack of information about the disk midplane temperature. Our estimate of the midplane disk temperature is made using the following simple irradiated flaring disk recipe:

$$T_d(r) = \left(\frac{\frac{1}{2}\varphi L_*}{4\pi r^2 \sigma_{\text{SB}}}\right)^{1/4} \quad (5)$$

where  $\sigma_{\text{SB}}$  is the Stefan-Boltzmann constant and  $\varphi$  is the so-called flaring angle (e.g. Chiang & Goldreich 1997; D’Alessio et al. 1998; Dullemond et al. 2001). The factor of  $1/2$  in front of the flaring angle  $\varphi$  originates from the consideration that the stellar radiation heats the surface layer of the disk, which then radiates half of that energy away and half into the deeper regions of the disk. Only the latter half goes into the energy balance equation between irradiation and radiative cooling of the disk interior. We take the flaring angle to be  $\varphi = 0.02$  which is an estimate based on typical values from models. In using this simple recipe we assume that the optical and in-

frared dust opacity is dominated by a population of small grains that is vertically more extended than the larger dust grains seen in the ALMA images. The two dust populations may be largely decoupled (see e.g. the BL-series of models of Dullemond & Dominik (2004) as an illustration). The value of  $\varphi = 0.02$  is nothing more than an educated guess, so its value can easily be wrong by a factor of four or so. But the fact that the pressure scale height goes as  $T_d^{1/2} \propto \varphi^{1/8}$  means that such an error only affects  $h_p$  mildly.

Assuming that the gas temperature is equal to the dust temperature, the pressure scale height of the disk now follows from  $h_p = \sqrt{k_B T_d r^3 / \mu m_p G M_*}$  with  $k_B$  the Boltzmann constant,  $m_p$  the proton mass,  $G$  the gravitational constant and  $\mu = 2.3$  the mean molecular weight in atomic units. The stellar parameters are taken from Table 1.

We see from Table 2 that some rings are narrower than the (estimated) pressure scale height  $h_p$ , while others are broader. This comparison is important because long-lived pressure bumps in the gas cannot be radially narrower than about one pressure scale height. If a thermal emission ring produced by the dust is substantially narrower than  $h_p$ , then some kind of dust trapping must have taken place. We can thus conclude that we have strong evidence of dust trapping operating in the rings of AS 209, Elias 24 and

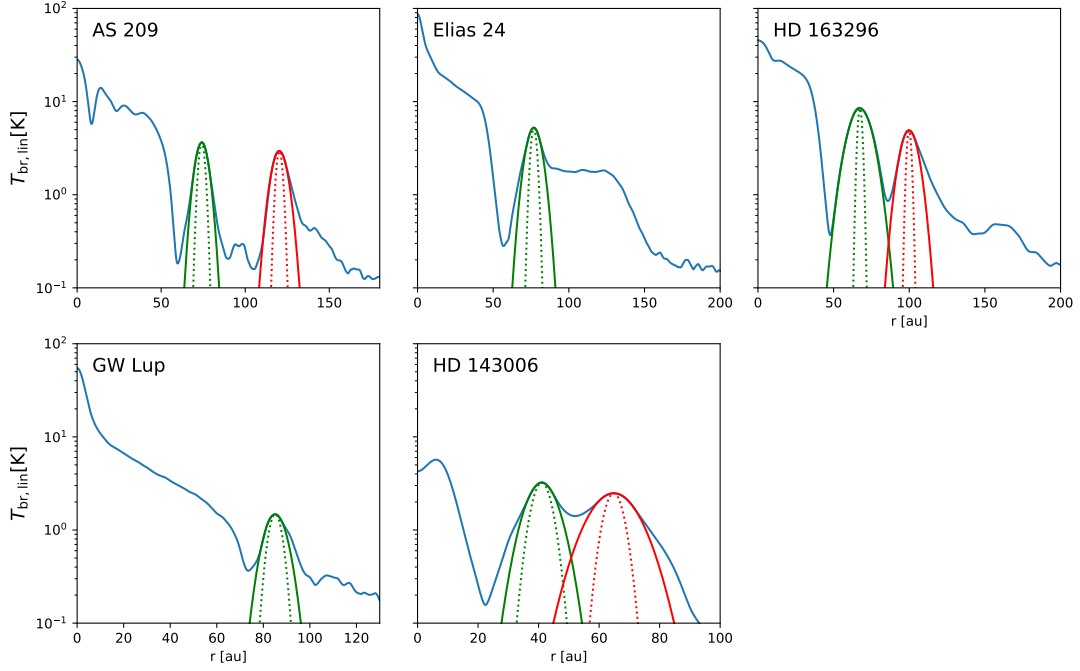


**Fig. 2.** The linear brightness temperature in band 6 of the five disks in our sample which have the most pronounced rings. The vertical axis is logarithmic to better show the contrast. The eight highest contrast rings are fitted by a Gaussian profile, shown as the solid inverse parabolas. The dotted inverse parabolas are Gaussians with the width of the ALMA beam. For a detailed description of these data, Guzmán et al. (2018) for AS 209, Isella et al. (2018) for HD 163296, and Huang et al. (2018) for the rest. **TODO: y-labels**

Source	Ring	beam [mas]	domain [au]	$A$ [K]	$A_{\text{dec}}$ [K]	$r_0$ [au]	FWHM [mas]	$\sigma$ [au]	$w_d$ [au]	$T_d$ [K]	$B_{\text{d}\nu}^{\text{lb}}$ [K]	$w_d/h_p$	$\tau_\nu^{\text{peak}}$	$M_d$ [ $M_\oplus$ ]
AS 209	1	37	69 – 79	3.64	4.18	74.1	75.4	3.87	3.38	15.8	10.9	0.6	0.48	28.5
AS 209	2	37	115 – 125	2.95	3.23	120.3	90.3	4.64	4.23	12.4	7.7	0.4	0.55	60.7
Elias 24	1	35	72 – 82	5.22	5.69	76.9	88.0	5.08	4.66	22.3	17.2	0.6	0.40	33.4
HD 163296	1	43	60 – 76	8.48	8.76	67.4	171.7	7.36	7.13	30.8	25.6	1.6	0.42	43.8
HD 163296	2	43	94 – 104	4.92	5.20	99.9	133.6	5.73	5.42	25.3	20.2	0.8	0.30	38.0
GW Lup	1	44	79 – 89	1.48	1.87	85.1	72.1	4.74	3.76	10.3	5.7	0.5	0.40	34.1
HD 143006	1	45	35 – 45	3.21	4.11	41.0	72.2	5.06	3.95	27.2	22.0	1.9	0.21	10.0
HD 143006	2	45	59 – 72	2.48	2.71	64.8	112.5	7.88	7.22	21.6	16.6	2.0	0.18	21.6

**Table 2.** The model parameters for the Gaussian ring fits in Figs. 2 and 3. The “beam” column gives the beam size (full-width-at-half-max). Given that in reality the beam is elliptic, and the disk has an inclination, this is merely an estimate. The “domain” column gives the radial domain within which the Gaussian fit was made.  $A$  is the peak linear brightness temperature of the best-fit Gaussian ring model,  $r_0$  is its radius in au, FWHM is the width expressed as full-width-at-half-maximum in units of milliarcsecond,  $\sigma$  is its width expressed as standard deviation in units of au and  $w_d$  is the width of the underlying (deconvolved) dust emission profile, also expressed as standard deviation in units of au. The  $A_{\text{dec}}$  column is like  $A$ , but corrected for the deconvolution (see Eq. 3). The last five columns are derived from a simple disk model assumption:  $T_d$  is the midplane temperature of the disk (we assume gas and dust temperature to be equal) computed from Eq. (5), assuming a flaring angle of  $\varphi = 0.02$ . From that one can derive the corresponding linear brightness temperature  $B_{\text{d}\nu}^{\text{lb}}$  using Eq. (A.6) for  $\nu = c/(0.13 \text{ cm})$  (ALMA band 6). The  $w_d/h_p$  column expresses the deconvolved dust ring width in units of the disk pressure scale height  $h_p$  computed from  $T_d$ . The  $\tau_\nu^{\text{peak}}$  column gives the estimated optical depth at the peak of the ring, calculated from Eq. (8). The last column is the computed dust mass in the ring in units of Earth masses. See Appendix F for details. In making these mass estimates we use the DSHARP dust opacity model (Birnstiel et al. (2018)) for a grain radius of  $a = 0.1 \text{ cm}$ , which yields an absorption opacity  $\kappa_\nu^{\text{abs}}(\lambda = 0.13 \text{ cm}) = 1.93 \text{ cm}^2/\text{g}$ . The uncertainty of the opacity value is, however, very large, since we do not know apriori the grain size distribution.

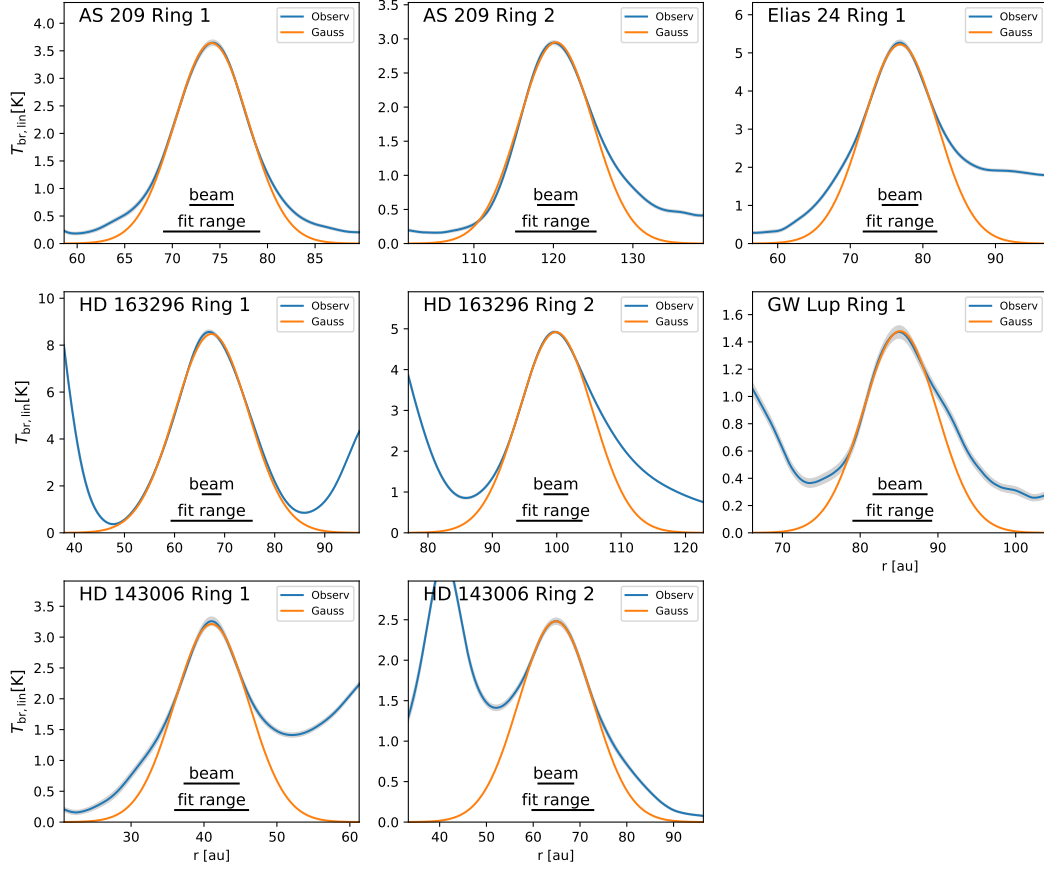


**Fig. 3.** Gaussian fits to the eight rings of this paper. The blue curves are the observations, the orange curves are the best fit Gaussian profiles. The “fit range” bar shows the radial range within which the Gauss was fitted to the data. The fit range was chosen to fit the part of the curve that, by eye, most resembles a Gaussian. The “beam” bar shows the FWHM beam size of the observations. The grey band around the blue curve shows the estimated uncertainty of the data. **TODO: y-labels**

GW Lup. For the other rings dust trapping is certainly not ruled out either, but would require further evidence.

For these observations the FWHM beam size for each ring is listed in Table 2. These are azimuthal average beam size values according to Eq. (A.2), based on the values listed in Huang et al. (2018). This number can be compared to the FWHM ring width in Table 2, and it shows that the widths of all the rings are spatially resolved. Some are only marginally resolved (AS 209 rings 1 and 2, GW Lup and the ring 1 of HD 143006), but the data are inconsistent with radially unresolved rings. For AS 209 this is confirmed by more detailed analysis in the uv-plane by Guzmán et al. (2018). **CHECK IF HUANG DOES THIS, TOO.**

These Gaussian profiles fit the observed data remarkably well, as can be best seen in Fig. 3. For the broad rings of HD 163296 the closeness to a Gaussian profile is particularly striking, given that these rings are resolved by many beam widths. For Elias 24 the ring fits a Gaussian near the peak, but deviates from Gaussian already less

half a width from the center. Likewise for the rings of HD 143006. The ring around GW Lup is an intermediate case, which fits a Gauss well on the inner flank, but rather badly on the outer flank.

In all ring profiles shown in Fig. 3 the observed profile rises above the Gaussian fit at some point in the wings. For the inner flanks of ring 1 of Elias 24 and ring 1 of HD 143006, as well as for the outer flanks of ring 2 of AS 209, ring 2 of HD 163296, the ring of GW Lup and ring 2 of HD 143006 the excess above the Gaussian gradually increases away from the peak of the Gaussian. Put differently, the profiles appear to deviate from Gaussian shape to pyramid-shape (or Lorentzian shape) in the flanks. This cannot be simply the addition of a constant background, because that would preserve the Gaussian shape, and merely lift it higher. Instead, while the core of the profile can clearly be well-described by a Gaussian, in the flanks there is a clear transition to a different, wider, shape.

A similar effect occurs between the two rings in HD 163296 and HD 143006, where in particular for HD 143006

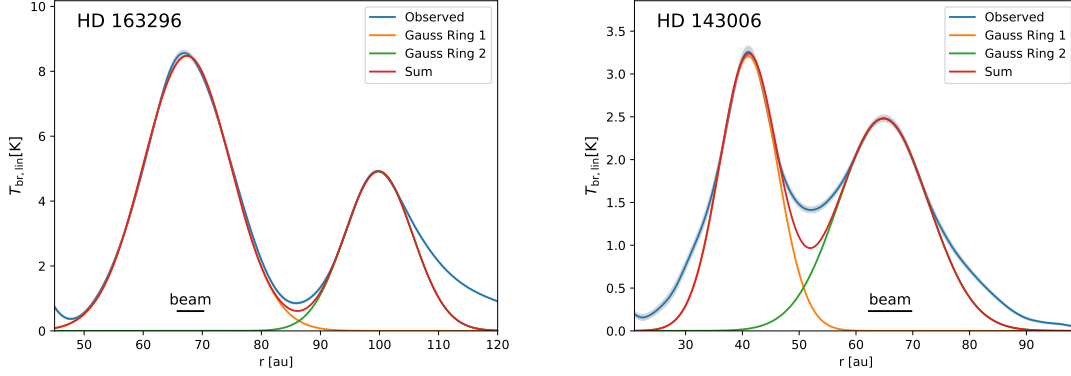


**Fig. 4.** The sum of the two Gaussian fits for the two sources with two partly overlapping rings: HD 163296 and HD 143006. **TODO: y-labels**

it is clear from Fig. 4 that it cannot be just the effect of the sum of the two Gaussians.

It is not immediately clear whether this is relevant or just chance. It lies in the nature of fitting a Gaussian profile to something non-Gaussian that there will be a region close to the peak where the curve fits the Gaussian reasonably well, while the deviation will increase the farther away from the peak one looks. This danger is particularly large in the present case, since the fitting range was chosen to maximize the similarity to the Gauss near the peak. Nevertheless, it clearly signals a deviation from Gaussian.

#### 4. Optically thin analysis

As a first guess, we will assume that we can ignore optical depth effects, i.e. that the thermal emission of the dust is optically thin. The linear brightness temperature profiles shown in Section 2, after deconvolution with the beam, are then linear maps of the spatial distribution of dust, if we ignore any temperature gradients across these rings. In other words: the deconvolved versions of the Gaussian fits of Section 3 (Eq. 4) will then directly translate in Gaussian models of the radial dust distribution.

The conversion between the deconvolved observed linear brightness temperature profile  $I_{\nu}^{\text{lb,dec}}(r)$  and the dust surface density profile  $\Sigma_d(r)$  is then

$$\Sigma_d(r) = \frac{I_{\nu}^{\text{lb,dec}}(r)}{\kappa_{\nu}^{\text{abs}} B_{\nu}^{\text{lb}}(T_d)} \quad (6)$$

where  $T_d$  is the temperature of the dust,  $\kappa_{\nu}^{\text{abs}}$  is the absorption opacity, and  $B_{\nu}^{\text{lb}}(T_d)$  is the Planck function expressed as linear brightness temperature (Eq. A.6).

By replacing  $I_{\nu}^{\text{lb,dec}}(r)$  with the Gaussian fit  $I_{\nu}^{\text{lb,gauss,dec}}(r)$  given by Eq. (4) we obtain the corresponding  $\Sigma_d^{\text{gauss}}(r)$  from Eq. (6). From this Gaussian model we can derive the total dust mass trapped in the ring:

$$M_d = \int_0^{\infty} 2\pi r \Sigma_d(r) dr \simeq \frac{(2\pi)^{3/2} r_0 A \sigma}{\kappa_{\nu}^{\text{abs}} B_{\nu}^{\text{lb}}(T_d)} \quad (7)$$

where we used the identity  $A \sigma = A_{\text{dec}} w_d$ .

We use the DSHARP opacity model (Birnstiel et al. (2018)) which, for a grain radius of  $a = 0.1 \mu\text{m}$  yields a dust opacity of  $\kappa_{\nu}^{\text{abs}}(\lambda = 0.13 \text{ cm}) = 1.93 \text{ cm}^2/\text{g}$ . The resulting dust mass estimates are listed in Table 2.

The main uncertainty lies in the uncertainty in the opacity value  $\kappa_{\nu}^{\text{abs}}$ . This value depends on the grain size (or grain size distribution) as well as many other factors including composition, grain shape and uncertainties in the method of computation of the opacity. We refer to Birnstiel et al. (2018) for a discussion of the opacity model used for the DSHARP campaign.

**[Discuss the minimum and maximum mass values]**

The other uncertainty, though much less severe, is the dust temperature  $T_d$ . From the continuum images we have no information about  $T_d(r)$ . From the CO line emission one can estimate the temperature in the disk surface layers, but not in the midplane (see e.g. Weaver et al. 2018). Instead, we will use the flaring angle recipe given by Eq. (5) with  $\varphi = 0.02$ . The resulting values of  $T_d$  at the peak of the rings are given in Table 2. For Eq. (6) we need the corresponding linear brightness temperature  $B_{\nu}^{\text{lb}} \equiv B_{\nu}^{\text{lb}}(T_d)$ , which is listed in the next column in Table 2.

Given the amplitude of the deconvolved Gauss fit  $A_{\text{dec}}$  (see Eq. 4), we can derive the optical depth  $\tau_{\nu}^{\text{peak}}$  of the ring at its peak at  $r = r_0$ :

$$\tau_{\nu}^{\text{peak}} = -\ln \left( 1 - \frac{A_{\text{dec}}}{B_{\nu}^{\text{lb}}(T_d)} \right) \quad (8)$$

This allows us to verify if our assumption of optical thinness is justified. The results are listed in Table 2. We conclude that the optically thin assumption is not entirely wrong, but not quite right either. The estimated dust surface density  $\Sigma_d$  and dust mass  $M_d$  derived from the optically thin assumption (Eqs. 6 and 7, respectively) are only mildly affected by the optical depth effects.

A much stronger effect on the conversion of the observations to dust mass remains the uncertainty of the opacity. As shown in Birnstiel et al. (2018) the value of



$\kappa_\nu^{\text{abs}} = 1.93 \text{ cm}^2/\text{g}$  that we use here can easily be wrong by a factor of 10 upward or a factor of 0.1 downward, with correspondingly large changes in the derived dust mass.

## 5. Optical depth effects

As we have seen in Section 4, the optical depth of these dust rings is not very low: about 0.2 and upward, usually around 0.4. For the case of HD 163296 there is evidence from the absorption of CO line emission from the back side of the disk that the optical depth in the two prominent rings is even close to unity, as shown by Isella et al. (2018). For simplicity we will perform most of our analysis of the later Sections using the optically thin approximation. But before doing that, it is important to investigate how strong the effect of optical depth is, and how it would affect our results. This is the topic of this Section.

### 5.1. Simple optical depth correction

Let us assume that the dust has zero albedo. Then the inclusion of the effect of optical depth is simple. We replace Eq. (6) with the formal transfer equation:

$$I_\nu^{\text{lb,dec}}(r) = e^{-\tau_\nu(r)} I_\nu^{\text{lb,bg}} + (1 - e^{-\tau_\nu(r)}) B_\nu^{\text{lb}}(T_d) \quad (9)$$

where  $\tau_\nu(r)$  is the optical depth profile across the ring, and  $I_\nu^{\text{lb,bg}}$  is the background brightness, either from background clouds or from the cosmic microwave background. In interferometric observations a flat background is Fourier-filtered out, but in the radiative transfer it plays a role in the non-linear optical depth regime ( $\tau_\nu \gtrsim 0.3$ ), even if we are only interested in the excess emission above the background  $I_\nu - I_\nu^{\text{lb,bg}}$ . We assume, however, that the cloud background emission is negligible. The linear brightness temperature of the cosmic background at  $\lambda = 0.13 \text{ cm}$  is  $I_\nu^{\text{lb,cmb}} = 0.195 \text{ K}$ . This is not negligible compared to the brightness temperatures in the inter-ring regions, but those regions are low optical depth regions, where the radiative transfer equation for  $I_\nu - I_\nu^{\text{lb,bg}}$  is linear and the background drops out. Only near the peak of the rings the optical depth becomes non-negligible, but the value of  $B_\nu^{\text{lb}} \equiv B_\nu^{\text{lb}}(T_d)$  is always much larger than the cosmic background value of 0.195 K (see Table 2). We will therefore ignore the background and set  $I_\nu^{\text{lb,bg}} = 0$  in Eq. (9) for simplicity.

To obtain the dust distribution we first compute  $\tau_\nu(r)$

$$\tau_\nu(r) = -\ln \left( 1 - \frac{I_\nu^{\text{lb,dec}}(r)}{B_\nu^{\text{lb}}(T_d)} \right) \quad (10)$$

which is identical to Eq. (8), but now for the entire profile instead of just for the peak. The profile for  $\Sigma_d(r)$  now follows from

$$\Sigma_d(r) = \frac{\tau_\nu(r)}{\kappa_\nu^{\text{abs}}} \quad (11)$$

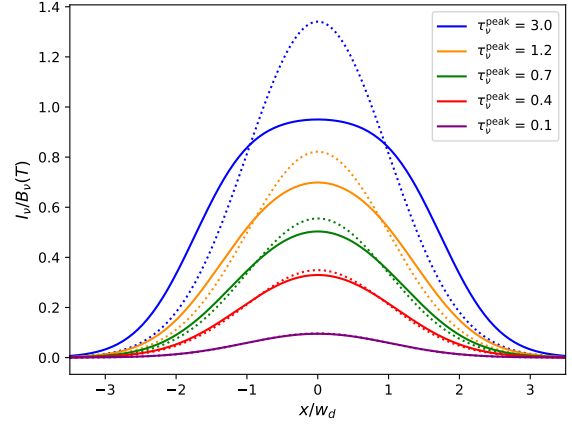


**Fig. 5.** The saturation effect of a gaussian emissivity profile at various peak optical depths. Solid curves: the result of the formal radiative transfer equation (Eq. 9 with background set to zero). Dotted curves: the unsaturated case, normalized to have the same total integral as the solid curves.

### 5.2. Saturation and flat-topped ring profiles

Given the non-linearity of Eq. (10), in particular near the peak of the ring profile, the resulting  $\Sigma_d(r)$  profile becomes non-Gaussian even if the measured  $I_\nu^{\text{lb,dec}}(r)$  has a Gaussian shape. Or put the other way: if  $\Sigma_d(r)$  is a Gaussian profile, the resulting  $I_\nu^{\text{lb,dec}}(r)$  will not: it will lead to a flattened top, where  $I_\nu^{\text{lb,dec}}(r)$  saturates to  $B_\nu^{\text{lb}}(T_d)$ . See Fig. 5 for a quantitative example.

The Gaussian fits of Section 3 suggest, however, that the  $I_\nu^{\text{lb,dec}}(r)$  profiles do not show clear signs of being flat-topped. A simple comparison to Fig. 5 shows that peak optical depths of  $\gg 1$  can be clearly excluded.

However, the deviation from true Gaussian becomes small for  $\tau_\nu \lesssim 1$ . It is therefore an important question how strongly we can exclude the flattening of the top of the peak, or in other words: how strong an upper limit we can set on  $\tau_\nu^{\text{peak}}$ . Can the flattening of the underlying Gaussian emissivity due to self-absorption be mistaken for a different Gaussian profile that is wider and lower than the underlying dust emissivity, because the deviations vanish within the errorbars on the measurements? We investigate this in detail in Appendix C. We find that up to  $\tau_\nu \lesssim 1$  the flattened-out profile can still be reasonably well fitted by a Gaussian function. This Gauss, of course, has a strongly reduced amplitude compared to the optically thin approximation: by a factor  $(1 - e^{-\tau_\nu^{\text{peak}}})/\tau_\nu^{\text{peak}}$ , before beam smearing, in order to mimic the self-absorption. Also, it has a slightly wider shape, but this is a small effect.

This means that, just from the analysis of the shape of the radial profiles of the rings, we can only exclude large optical depth ( $\tau_\nu^{\text{peak}} \gg 1$ ), but not mild optical depth  $\tau_\nu^{\text{peak}} \simeq 0.3 \dots 1$ . The optically thin treatment, as we will adopt in Section 6 and onward, could there-

fore lead to ignoring optical depth effects of the order of  $(1 - e^{-\tau_\nu^{\text{peak}}})/\tau_\nu^{\text{peak}}$ , which amounts to an underestimation of dust mass of up to 37% for  $\tau_\nu^{\text{peak}}$  up to 1.

There is, however, another way to constrain these optical depth effects. As we have already seen in Section 3: given the measured linear brightness temperature  $I_\nu^{\text{lb,obs}}$ , and given a dust temperature  $T_d$ , the optical depth follows immediately. In other words: a larger optical depth than given in Table 2 requires a lower dust temperature than given in that table. These temperature estimates are already on the low side, by assuming the somewhat low value of the flaring angle  $\varphi = 0.02$  in Eq. (5). It requires a quite strong reduction of  $\varphi$  to reduce the temperature sufficiently to increase the  $\tau_\nu^{\text{peak}}$  from Table 2 to unity. As an example let us take ring 1 of HD 163296 with  $T_d = 30.8$  K and  $\tau_\nu^{\text{peak}} = 0.42$  according to Table 2. According to Eq. (8), if we set  $\tau_\nu^{\text{peak}} = 1$ , we obtain from  $A_{\text{dec}} = 8.76$  the value  $B_\nu^{\text{lb}}(T_d) = 13.9$  K, corresponding, via Eq. (A.6) to  $T_d = 18.9$  K. This temperature is almost twice as low as the original estimate, and would require, according to Eq. (5), a flaring angle of  $\varphi = 0.00082$ . Such a flaring angle is unreasonably low and it invalidates the simple flaring angle recipe in the first place. Instead we would need to perform detailed 2-D/3-D radiative transfer calculations of the disk to investigate if such a low temperature is physically attainable. Or equivalently, such a study may allow us to find a theoretical lower limit to the dust temperature, which then translates into an upper limit to the  $\tau_\nu^{\text{peak}}$ . Alternatively, and possibly more reliably, if we obtain a high-resolution map in a second band, we can investigate the behavior of the spectral index over the radial profile of the rings, which also provides information about the optical depth.

### 5.3. The effect of scattering albedo

If the dust grains have a radius  $a$  comparable to the wavelength of our observations, the scattering albedo can be quite high. This means that the absorption optical depth can be substantially lower than unity, even if the full extinction optical depth (absorption plus scattering) is unity or larger. The near-unity extinction found in HD 163296 by Isella et al. (2018) from the CO maps could thus be compatible with the sub-unity absorption optical depth we derived in our Gaussian fitting procedure (see Table 2).

In fact, staying with the case of HD 163296, if we would assume that the albedo is zero, i.e. that the measured extinction optical depth from the CO maps equals the absorption optical depth, then we would find rather low dust temperatures at the location of the rings, which may be hard to explain theoretically, as shown in Section 5.2. If, however, part of the extinction is due to scattering, then it is easier to remain consistent with the dust temperature estimated from the flaring angle recipe.

However, when scattering is included, the radiative transfer becomes more complex than a simple use of a fac-

tor  $1 - e^{-\tau_\nu}$ . For completeness we describe, in Appendix D, an approximate solution to this problem for a thin slab model. In principle one would have to replace, in the above sections, as well as in Appendix C, all instances of  $1 - e^{-\tau_\nu}$  with the more detailed radiative transfer model of Appendix D. But to avoid too much complexity in this paper, we leave this to an interested reader.

### 5.4. Why are most rings so “fine-tuned”?

It is rather striking that in the analysis of the rings up to this point we have found several rather “fine-tuned” properties. For instance, the rings of AS 209, Elias 24, GW Lup and the inner ring of HD 143006 have a width that is only roughly twice the beam size (between 1.5 and 2.4 times, to be precise), but none are unresolved. Given the small sample it is very well possible that this is just coincidence. The fact that some rings (in particular those of HD 163296) are clearly much wider, lends some support to this.

The derived peak optical depths for most sources (except HD 143006), assuming our model of the dust temperature is correct, hover around 0.4, i.e. just in between the optically thin and optically thick regime. Is this coincidence as well, or is there a deeper reason behind this? In this paper we have focussed on the strongest, most isolated rings in the DSHARP sample, which could mean that this is a selection effect.

Finally, all ring profiles are remarkably similar to a Gaussian shape. On the one hand, this may be something similar to the effect discussed in Section 5.2 and Appendix C. And with some rings being only about two beams wide, any ‘peaklike’ shape will tend to look similar to a Gaussian. On the other hand, the two rings of HD 163296 are resolved by more than 3 beams, yet they show a Gaussian shape well into the wings.

Could it be that some observational or data reduction effect may have smeared out our data more than expected? We have, to the best of our abilities, been unable to identify such an effect. And, as described in Appendix XXXX, we have performed a full self-test cycle of a mock ring being processed through our pipeline, and found no excessive smearing-out, nor effects that would skew our conclusion that the rings indeed have an intrinsically Gaussian profile. It seems that these “fine-tuned” properties of the rings are real.

## 6. The rings as dust traps

The hypothesis we are now going to test is that the rings are caused by dust trapping in axisymmetric pressure bumps. For simplicity we will assume that the radial gas pressure profile is fixed in time, and there is no back reaction of the dust onto the gas. The pressure bump is assumed to be so strong that the dust trapping in these rings is nearly perfect: no dust escapes. We then expect that the dust distribution finds an equilibrium between dust drift and turbulent spreading. Low turbulence will



lead to thinner dust rings than high turbulence. For simplicity we shall assume the gas pressure bump to have a Gaussian radial profile with its peak at radius  $r_0$  and width  $w \ll r_0$ . This problem can be solved analytically.

### 6.1. Model

Consider the following radial Gaussian profile for the pressure at the disk midplane:

$$p(r) = p_0 \exp\left(-\frac{(r - r_0)^2}{2w^2}\right) \quad (12)$$

We will discuss the hydrodynamic stability of a gas distribution arranged in this way in Section E.5. But for now we will not be concerned with that and we will assume the pressure-profile of Eq. (12) to be given and fixed.

In Appendix E we derive that, for our purposes, a good approximation of the stationary dust distribution within the dust trap is:

$$\Sigma_d(r) = \Sigma_{d0} \exp\left(-\frac{(r - r_0)^2}{2w_d^2}\right) \quad (13)$$

where

$$w_d = w (1 + \psi^{-2})^{-1/2} \quad (14)$$

with  $\psi$  given by

$$\psi = \sqrt{\frac{\alpha_{\text{turb}}}{\text{Sc St}}} \quad (15)$$

Here  $\text{St}$  is the Stokes number of the dust particles (Eq. E.3),  $\text{Sc}$  is the Schmidt number of the turbulence in the gas, and  $\alpha_{\text{turb}}$  is the usual turbulence parameter. Note that this solution is for a single grain size.

For large grains and/or weak turbulence one finds  $\psi \ll 1$ , which leads to  $w_d \ll w$ . In this case the dust is strongly trapped near the peak of the pressure bump. The opposite is the case for small grains and/or strong turbulence, for which one gets  $\psi \gg 1$ , which leads to  $w_d \rightarrow w$ . In this case the trapping is very weak and the dust-to-gas ratio within the pressure bump stays constant. Only in the very wings of the Gaussian pressure bump is dust trapping significant, but this effect can only be studied using the more accurate non-gaussian solution of Eq. (E.13). We will return to the dust trapping effect in the wings in Section XXXXX.

Eq. (13) has only two parameters:  $\Sigma_{d0}$  and  $w_d$ . Both can be fairly directly measured from the observations, though  $\Sigma_{d0}$  will depend on the opacity, and hence on the unknown grain size (see discussion in Appendix F). The values of  $w_d$  for the rings in our sample can be directly taken from Table 2.

The width of the dust ring  $w_d$  is physically set by  $\alpha_{\text{turb}}$ ,  $\text{Sc}$ ,  $\text{St}$  and  $w$  through the above equations. We therefore have one observational value for four unknown parameters. This is heavily degenerate. All we can do is to test if the measured value of  $w_d$  is consistent with expected values of  $\alpha_{\text{turb}}$ ,  $\text{Sc}$ ,  $\text{St}$  and  $w$ .

### 6.2. Ranges of $\alpha_{\text{turb}}$ , $\text{Sc}$ , $\text{St}$ and $w$

Reasonable values of  $\alpha_{\text{turb}}$ ,  $\text{Sc}$ ,  $\text{St}$  and  $w$  obey certain restrictions. First of all, the Schmidt number  $\text{Sc}$  is merely a way to relate the turbulent viscosity with the turbulent mixing. If we do not strive to learn about the turbulent viscosity, and instead are satisfied with learning only about the turbulent mixing, then we are only interested in the combination  $\alpha_{\text{turb}}/\text{Sc}$ . For simplicity we set  $\text{Sc} = 1$ .

The value of the turbulence parameter  $\alpha_{\text{turb}}$  is usually considered to be between  $10^{-6} \lesssim \alpha_{\text{turb}} \lesssim 10^{-2}$ .

The width of the pressure bump cannot be smaller than about a pressure scale height, but also not smaller than the width of the dust ring. Therefore  $w_{\text{min}} = \max(h_p, w_d)$ . In the case of the double rings (AS 209, HD 163296 and HD 143006), the full-width-at-half-maximum  $2.355 w$  should not exceed the radial separation of the rings. For the two single ring sources we take the deepest point of the gap to the inside of the ring as the upper limit on the half-width-at-half-maximum  $1.178 w$ . These lower and upper limits on  $w$  are listed in Table 3.

The Stokes number  $\text{St}$  can be any value. But it is directly related to the grain size  $a$  and the gas density  $\rho_g$ , where the gas density is directly related to the gas surface density  $\Sigma_g$  via  $\Sigma_g = \sqrt{2\pi} h_p \rho_g$ . If we have observational constraints on  $a$  and a good estimate of the gas surface density  $\Sigma_g$ , then we can eliminate this uncertainty, and we are left with two unknown parameters ( $\alpha_{\text{turb}}$  and  $w$ ) for one measurement ( $w_d$ ). Unfortunately, while estimating  $a$  from observations may be doable, it is far more difficult to estimate  $\Sigma_g$ . Standard disk gas mass estimates are of limited use, as they are based on measuring the dust mass and multiplying it by the estimated gas-to-dust ratio. Since we are testing the hypothesis of dust trapping, we cannot assume a standard gas-to-dust ratio.

One can, however, set an upper bound on  $\Sigma_g$  by demanding that the disk is gravitationally stable, i.e. that the Toomre parameter obeys

$$Q_{\text{Toomre}} \equiv \frac{c_s \Omega_K}{\pi G \Sigma_g} > 2 \quad (16)$$

Here  $c_s = \sqrt{k_B T / \mu m_p}$  is the isothermal sound speed, with  $k_B$  the Boltzmann constant,  $m_p$  the proton mass, and  $\mu = 2.3$  the mean molecular weight in atomic units.  $\Omega_K = \sqrt{GM_*/r^3}$  is the Kepler frequency,  $G$  is the gravitational constant and, finally,  $\Sigma_g$  the gas surface density. Taking the disk midplane temperature from Table 2, which was calculated using Eq. (5), we can compute the upper limits on  $\Sigma_g$  for all of the rings. The results are given in Table 3.

One can estimate a lower limit to the gas density by demanding that the gas surface density must be at least as large as the dust surface density, since dust trapping is unlikely to achieve a larger concentration of dust than that. Depending on which of the two opacities we use (see Appendix F) we arrive at different estimates of  $\Sigma_d(r = r_0)$ . By demanding  $\Sigma_g \gtrsim \Sigma_d$  we arrive at two lower limits of the gas surface density, given in Table 3. It

Source	Ring	$w_{\min}$ [au]	$w_{\max}$ [au]	$\Sigma_{g,\min,iv}$ [g/cm <sup>3</sup> ]	$\Sigma_{g,\min,ri}$ [g/cm <sup>3</sup> ]	$\Sigma_{g,\max}$ [g/cm <sup>3</sup> ]	$a_{\max}$ [cm]	$St_{(a=0.02\text{ cm})}$ (for $\Sigma_{g,\max}$ )	$\alpha/St$ (for $w_{\max}$ )	$\alpha/St$ (for $w_{\min}$ )	$\alpha_{\text{exmp}}$
AS 209	1	5.59	19.6	1.1e-02	2.0e-01	1.6e+01	15.7	3.9e-03	3.1e-02	5.7e-01	1.2e-04
AS 209	2	10.25	19.6	1.2e-02	2.3e-01	6.9e+00	5.8	9.1e-03	4.9e-02	2.1e-01	4.4e-04
Elias 24	1	7.26	17.1	9.7e-03	1.8e-01	1.8e+01	18.8	3.6e-03	8.0e-02	7.0e-01	2.9e-04
HD 163296	1	7.13*	13.8	1.1e-02	1.9e-01	4.1e+01	40.0	1.5e-03	3.6e-01	–	5.6e-04
HD 163296	2	7.07	13.8	7.8e-03	1.4e-01	2.0e+01	27.3	3.1e-03	1.8e-01	1.4e+00	5.6e-04
GW Lup	1	7.49	9.9	8.3e-03	1.5e-01	7.8e+00	9.8	8.0e-03	1.7e-01	3.4e-01	1.3e-03
HD 143006	1	3.95*	10.1	4.7e-03	8.6e-02	7.5e+01	167.1	8.4e-04	1.8e-01	–	1.5e-04
HD 143006	2	7.22*	10.1	4.8e-03	8.8e-02	3.4e+01	73.1	1.9e-03	1.0e+00	–	1.9e-03

**Table 3.** Limits on the free parameters of the dust trapping model. The lower limit to the pressure bump width  $w_{\min}$  is the pressure scale height  $h_p$ . If, however, the width of the dust ring  $w_d > h_p$ , then the lower limit is  $w_d$  (marked with the symbol \*). The upper limit  $w_{\max}$  is derived from the separation between the rings (for AS 209, HD 163296 and HD 143006) or from the separation of the ring to the nearest minimum (for Elias 24 and GW Lup). The two lower limits on the gas surface density  $\Sigma_g$  were derived by demanding  $\Sigma_g \gtrsim \Sigma_d$ , where  $\Sigma_d$  was computed in Appendix F using two different opacities: that of Ivezić et al. (leading to  $\Sigma_{g,\min,iv}$ ) and that of Ricci et al. (leading to  $\Sigma_{g,\min,ri}$ ). The column marked with  $\Sigma_{g,\max}$  is the upper limit on the gas surface density derived from demanding that the gas disk is gravitationally stable. The  $a_{\max}$  column is the maximum grain size for which the derived dust surface density together with the gas surface density remain gravitationally stable. The  $St_{(a=0.02\text{ cm})}$  column gives an example value of the Stokes number: it is the value of  $St$  if the grains have a radius of 0.02 cm, for the case of  $\Sigma_g = \Sigma_{g,\max}$ . The two columns for  $\alpha/St$  are derived for the widest and narrowest gas bump, respectively. The column  $\alpha_{\text{exmp}}$  is the value of  $\alpha_{\text{turb}}$  for an example choice of parameters:  $w = w_{\max}$ ,  $\Sigma_g = \Sigma_{g,\max}$  and  $a = 0.02\text{ cm}$ .

is likely that even for much larger values of the gas surface density the dust-gas mixture becomes unstable to the streaming instability and other types of instabilities. If we can convince ourselves that such instabilities are not operating in these rings, then this puts a substantially stronger (i.e. larger) lower limit on the gas surface density.

Also if the grains are much larger than  $\lambda/(2\pi) \simeq 0.02\text{ cm}$ , the opacity drops and the resulting dust surface density estimate increases, yielding larger lower limits to the gas density.

Along this line of thinking one can compute the largest grain radius for which the Toomre parameter of the disk stays above 2. We use the Ivezić opacity for that, which, for large grains, has similar values as the Ricci opacity. This leads to values of several centimeters to half a meter (Table 3). Again these are conservative limits, with real values likely to be substantially smaller. **UPDATE THESE VALUES AND RICCI NAME SINCE WE NOW USE DIFFERENT OPACITY MODEL.**

### 6.3. Application to the observed rings

We now wish to apply the model of Subsection 6.1 with the limits on the parameter ranges derived in Subsection 6.2 to the observed ring widths  $w_d$  listed in Table 2.

From an assumed value of  $w$  and the measured value  $w_d$  we can directly compute the ratio  $\alpha_{\text{turb}}/St$

$$\frac{\alpha_{\text{turb}}}{St} \equiv \psi^{-2} = \left[ \left( \frac{w}{w_d} \right)^2 - 1 \right]^{-1} \quad (17)$$

where we used Eqs. (14, 15), and set  $Sc = 1$ . We will consider two choices of  $w$ : the  $w_{\min}$  and  $w_{\max}$  from Table 3.

For the choice  $w = w_{\max}$  (the widest possible pressure bump) the dust rings are all narrower than the gas rings:  $w_d < w$ , which implies that the dust trapping is operational, and Eq. (17) gives information about the turbulent strength. For the choice  $w = w_{\min}$  (the narrowest possible pressure bump) we can only use Eq. (17) for the rings for which  $w_d < h_p$ . The reason is that for those rings with  $w_d > h_p$  (marked with a \* in Table 3) the minimal pressure bump width is  $w_{\min} = w_d$ , and the dust ring is as wide as the pressure bump, implying that dust trapping is weak or non-operational. Any increase of  $\alpha_{\text{turb}}/St$  will keep  $w_d = w_{\min}$ , so one cannot derive any value for  $\alpha_{\text{turb}}/St$ . But for other rings we can compute  $\alpha_{\text{turb}}/St$ . The resulting values for both choices of pressure bump width are given in Table 3. They can be understood as the lower and upper limit on  $\alpha_{\text{turb}}/St$ .

The next task is to convert from Stokes number  $St$  to grain size  $a$ . The Epstein regime is valid for the typical grains we are interested in (less than a meter in size), in which case  $a$  and  $St$  are related by

$$St = \frac{\pi \xi_{\text{dust}} a}{2 \Sigma_g} \quad (18)$$

where  $\Sigma_g$  is the gas surface density and  $\xi_{\text{dust}}$  is the material density of the dust grains. Given that grains are expected to be a mixture of silicate, amorphous carbon and water ice, a value of  $\xi_{\text{dust}} \simeq 2\text{ g/cm}^3$  is reasonable.

To get a feeling for the results, let us choose the grain size to be  $a = 0.02\text{ cm}$ , which corresponds to  $\lambda/2\pi$  for

$\lambda = 0.13$  cm (the wavelength of ALMA band 6). The corresponding Stokes numbers, for the most massive possible gas disk ( $\Sigma_g = \Sigma_{g,\max}$ ), are listed in Table 3. This then allows us to convert the value of  $\alpha_{\text{turb}}/\text{St}$  into a value of  $\alpha_{\text{turb}}$ . For the case  $w = w_{\max}$  this leads to values  $\alpha_{\text{turb}} = 10^{-4} \dots \text{few} \times 10^{-3}$ , listed in Table 3 (column  $\alpha_{\text{expmp}}$ ).

These low values of  $\alpha_{\text{turb}}$  are consistent with the low values or upper limits reported recently (Pinte et al. 2016; Flaherty et al. 2018) [more?]. However, it has to be kept in mind that the values of  $\alpha_{\text{turb}} = \alpha_{\text{expmp}}$  were derived for an example choice of parameters:  $w = w_{\max}$ ,  $\Sigma_g = \Sigma_{g,\max}$  and  $a = 0.02$  cm. For a smaller value of  $w$ , a lower value of  $\Sigma_g$ , or larger grains, the computed value of  $\alpha_{\text{turb}}$  will increase. So that it is hard to set a true upper limit on  $\alpha_{\text{turb}}$  from these observations.

This seems to be in conflict with the results found by Pinte et al. (2016) who, from measuring an upper limit on the vertical extent of the dust, imply an upper limit on  $\alpha_{\text{turb}}$  of  $3 \times 10^{-3}$ . [IMPORTANT: We have to find out why Pinte et al. find this limit. Do they have additional constraints? Why can't they increase the grain size indefinitely? What are the constraints Eric and Andrea find for the similar analysis of HD 163296?]

Can we derive a *lower* limit to  $\alpha_{\text{turb}}$ ? This depends on whether we have information about the grain size. At present we have only the high resolution data for band 6, so we do not yet have information about the radial profile of the spectral slope. But in several recent observations of the spectral index across ringed disks (ALMA Partnership et al. 2015; Huang et al. 2018) one clearly sees that  $\alpha_{\text{spec}}$  varies across these rings, being closer to 2 at the ring center and substantially larger between the rings. This makes sense in terms of the dust trapping scenario in which we expect larger grains to be trapped more efficiently (and thus dominate the peak of the ring) than smaller grains, because the smaller grains will be more subject to turbulent mixing. This scenario requires a grain size distribution, so that the width of the dust ring is smaller for the bigger grains and bigger for the smaller ones. We will discuss our model in the context of grain size distributions in Section 6.4. But assuming that future data will also show similar spectral slope changes for our sources, we can already conclude that the grains trapped in the rings must have sizes larger than  $\lambda/2\pi = 0.02$  cm. The measured (resolved) width of the dust ring  $w_d$  then implies a lower limit to  $\alpha_{\text{turb}}$ . The value  $\alpha_{\text{turb}} = \alpha_{\text{expmp}}$  is then, in fact, this lower limit. We will, however, have to wait until high resolution ALMA data in another band becomes available to verify the minimal grain size of 0.02 cm.

Should the low spectral slope at the peak of the rings be confirmed, then the lower limits on  $\alpha_{\text{turb}}$  from the  $\alpha_{\text{expmp}}$  column in Table 3 paint a different picture from the low-turbulence picture that has emerged in recent times. The values of a few times  $10^{-4}$  to a few times  $10^{-3}$  are low, but they are only lower bounds. It would be somewhat unlikely if all rings have parameters at this extreme size

of parameter space, and it is therefore likely that  $\alpha_{\text{turb}}$  is easily a factor of ten higher or so. This would imply that protoplanetary disks are substantially turbulent after all. But to confirm this, we need to dig a bit deeper by including size distributions (Section 6.4) and non-perfect (“leaky”) dust traps (Section XXXX).

**We can make predictions for pressure slopes in CO**

## CONSIDER PRESSURE OFFSET!

### 6.4. Including a grain size distribution

[Here we will move away from a single grain size and see if we can understand the deviations from Gaussian by a grain size distribution]

## 7. Streaming instability, clumping, and the spectral index

[This section is temporarily hidden, because a lot still has to be done on this. Maybe it should be removed and put into a future paper.]

## 8. Discussion

### 8.1. Condition for the streaming instability

In the literature it is often mentioned that the streaming instability requires a dust-to-gas surface density ratio of  $\Sigma_d/\Sigma_g \gtrsim 0.02$  or higher to operate XXXXXXXX. This can, however, not be directly compared to our models, because this value of 0.02 was found for models without any pre-determined turbulence. The turbulence in those models was induced by the streaming instability itself or, if the streaming instability does not operate, by the Kelvin-Helmholtz instability (XXXX). In the analytic model of this Section, on the other hand, we set the turbulence strength by hand, by setting  $\alpha_{\text{turb}}$  to some value. In essence, we assume that there is another source of turbulence, such as the magnetorotational instability (XXXX) or the vertical shear instability (XXXX), that determines the mixing of the dust in the disk.

According to Youdin & Goodman (2005) the true criterion for the onset of the streaming instability is the ratio of dust and gas *volume* densities  $\rho_d/\rho_g \gtrsim 1$ . For a given surface density ratio  $\Sigma_d/\Sigma_g$ , the midplane volume density ratio, for a single grain species with midplane Stokes number  $\text{St} \ll 1$ , depends on the turbulent strength as

$$\frac{\rho_d}{\rho_g} \simeq \left(1 + \frac{\text{St}}{\alpha_{\text{turb}}}\right) \frac{\Sigma_d}{\Sigma_g} \quad (19)$$

The criterion of  $\Sigma_d/\Sigma_g \gtrsim 0.02$  mentioned in the literature thus relates to the criterion  $\rho_d/\rho_g \gtrsim 1$  via the turbulent strength and the Stokes number. Given that we do not compute the turbulent strength but prescribe it, we should rely on the more fundamental volume density criterion of Youdin & Goodman (2005) to assess whether the dust in our model triggers the streaming instability or not.

In our analytic setup of Section **CHECK** the dust ring is about 5 times narrower than the gas bump. Assuming that initially the dust-to-gas ratio was 0.01, this implies a dust-to-gas surface density ratio at the peak of the ring of 0.05, which is in excess of the usual 0.02 value. But as long as  $St \lesssim 19\alpha_{\text{turb}}$ , Eq. (19) shows that the mid-plane volume density ratio still stays below unity and no streaming instability sets in.

### 8.2. Can a resolved ring be in fact a blend of several unresolved rings?

Measuring the width of rings with finite-resolution observations is, of course, limited to ring widths that are larger than the “beam”. However, even for cases where the ring width clearly exceeds the beam size by a factor of a few or more, one may ask the question: is the wide ring we see truly a single wide ring, or could it also be made up of a series of spatially unresolved rings that are blended into a single wide ring due to the beam convolution? This question is particularly relevant for the very wide rings of HD 163296. It is, of course, hard to answer in general, since we have no observational means to test this.

But from the perspective of particle trapping by a pressure bump this question can be rigorously answered. A long-lived radial pressure perturbation in a protoplanetary disk cannot be much narrower than about a pressure scale height  $h_p(r)$ . **[Perhaps we should add an appendix where we use the stability criteria to rigorously put limits on the width and depth of the rings (even a wide ring will, deep in the gaussian wings, become unstable), and link this to a leakage of dust out of the trap.]**

A dust ring produced by dust trapping in this pressure bump may become rather narrow, dependent on a variety of parameters, as discussed in Section E. But there can not be more than a single such dust ring in each pressure bump.

For the wide rings of HD 163296 the pressure scale height, even under the most optimistically low disk temperature (e.g. 10 K) the pressure scale height at rings 1 and 2 are 2.4 au and 4.3 au, respectively, which correspond to FWHM widths of 55 and 101 milliarcseconds, respectively (where we have multiplied by 2.355 to obtain the full-width at half-maximum corresponding to a gaussian with  $h_p$  as standard deviation width). Clearly the ALMA observations in band 6, with FWHM beam size of 35 mas, spatially resolve the pressure scale height. This means that the ring separation will be spatially resolved by ALMA, ruling out the possibility that the wide rings are made up of a multitude of narrow rings, at least in the dust trapping scenario.

**[Add discussion of the plateau of Elias 24]**

### 8.3. Interpretation of the millimeter flux in terms of grain size

A common rule of thumb for interpreting millimeter and sub-millimeter fluxes and intensities from thermal dust emission is that you “observe the grain size equal to the wavelength you observe at”. This rule is based on the tendency of the dust opacity derived from a Mie calculation to peak at wavelength around  $\lambda \sim 2\pi a$ , with  $a$  the grain radius. For  $\lambda \ll 2\pi a$  the opacity becomes nearly constant while  $\lambda \gg 2\pi a$  it drops. This effect is even stronger for the scattering opacity. The validity of this rule of thumb relies, however, on the grain size distribution itself. For the simple **Ivezic et al. (1997)** opacity law, it is only valid for grain size distribution powerlaws obeying **XXXXXXXXXXXX**. **[TODO: Maybe here do an experiment with full opacity laws.]**

*Acknowledgements.* The authors acknowledge support by the High Performance and Cloud Computing Group at the Zentrum für Datenverarbeitung of the University of Tübingen, the state of Baden-Württemberg through bwHPC and the German Research Foundation (DFG) through grant no INST 37/935-1 FUGG. This research was initiated at the “Stars, Planets and Galaxies” meeting at the Harnackhaus in Berlin, April 2018. Part of this work was also funded by the DFG Forschergruppe FOR 2634 “Planet Formation Witnesses and Probes: Transition Disks”.

## References

- ALMA Partnership, Brogan, C. L., Pérez, L. M., et al. 2015, ApJL, 808, L3
- Andrews, S. M., Wilner, D. J., Hughes, A. M., Qi, C., & Dullemond, C. P. 2009, ApJ, 700, 1502
- Andrews, S. M., Wilner, D. J., Zhu, Z., et al. 2016, ApJL, 820, L40
- Barge, P. & Sommeria, J. 1995, A&A, 295, L1
- Benisty, M., Stolker, T., Pohl, A., et al. 2017, A&A, 597, A42
- Birnstiel, T., Dullemond, C. P., & Brauer, F. 2010, A&A, 513, A79
- Brauer, F., Dullemond, C. P., Johansen, A., et al. 2007, A&A, 469, 1169
- Casassus, S., van der Plas, G., M, S. P., et al. 2013, Nature, 493, 191
- Chiang, E. I. & Goldreich, P. 1997, ApJ, 490, 368
- Cieza, L. A., Casassus, S., Pérez, S., et al. 2017, ApJL, 851, L23
- D’Alessio, P., Cantö, J., Calvet, N., & Lizano, S. 1998, ApJ, 500, 411
- Dong, R., Zhu, Z., Fung, J., et al. 2016, ApJL, 816, L12
- Dubrulle, B., Morfill, G., & Sterzik, M. 1995, Icarus, 114, 237
- Dullemond, C. P. & Dominik, C. 2004, A&A, 421, 1075
- Dullemond, C. P. & Dominik, C. 2004, Astronomy & Astrophysics, 417, 159
- Dullemond, C. P., Dominik, C., & Natta, A. 2001, ApJ, 560, 957

- Fedele, D., Carney, M., Hogerheijde, M. R., et al. 2017, *A&A*, 600, A72
- Fedele, D., Tazzari, M., Booth, R., et al. 2018, *A&A*, 610, A24
- Flaherty, K. M., Hughes, A. M., Teague, R., et al. 2018, *ApJ*, 856, 117
- Foreman-Mackey, D., Hogg, D. W., Lang, D., & Goodman, J. 2013, *Publications of the Astronomical Society of the Pacific*, 125, 306
- Fromang, S. & Nelson, R. P. 2009, *A&A*, 496, 597
- Huang, J., Andrews, S. M., Cleeves, L. I., et al. 2018, *ApJ*, 852, 122
- Isella, A., Guidi, G., Testi, L., et al. 2016, *Physical Review Letters*, 117, 251101
- Ishimaru, A. 1978, *Wave propagation and scattering in random media*. Vol. 1.
- Ivezic, Z., Groenewegen, M. A. T., Men'shchikov, A., & Szczerba, R. 1997, *MNRAS*, 291, 121
- Klahr, H. H. & Henning, T. 1997, *Icarus*, 128, 213
- Kretke, K. A. & Lin, D. N. C. 2007, *ApJL*, 664, L55
- Marino, S., Perez, S., & Casassus, S. 2015, *ApJL*, 798, L44
- Pinilla, P., Benisty, M., & Birnstiel, T. 2012a, *A&A*, 545, A81
- Pinilla, P., Birnstiel, T., Ricci, L., et al. 2012b, *A&A*, 538, A114
- Pinte, C., Dent, W. R. F., Ménard, F., et al. 2016, *ApJ*, 816, 25
- Powell, D., Murray-Clay, R., & Schlichting, H. E. 2017, *ApJ*, 840, 93
- Rybicki, G. B. & Lightman, A. P. 1986, *Radiative Processes in Astrophysics*, 400
- Testi, L., Natta, A., Shepherd, D. S., & Wilner, D. J. 2003, *A&A*, 403, 323
- van der Marel, N., van Dishoeck, E. F., Bruderer, S., et al. 2013, *Science*, 340, 1199
- Weaver, E., Isella, A., & Boehler, Y. 2018, *ApJ*, 853, 113
- Whipple, F. L. 1972, in *From Plasma to Planet*, ed. A. Elvius, 211
- Youdin, A. N. & Goodman, J. 2005, *ApJ*, 620, 459
- Youdin, A. N. & Lithwick, Y. 2007, *Icarus*, 192, 588

## Appendix A: Conventions on brightness

The intensity of an interferometrically produced image at (sub-)millimeter wavelengths can be expressed in numerous ways. We will define our symbols here to avoid confusion. Expressed in CGS units, the intensity  $I_\nu$  at frequency  $\nu$  has dimension  $\text{erg cm}^{-2} \text{s}^{-1} \text{Hz}^{-1} \text{ster}^{-1}$ . From an observational point of view it is convenient to express it instead in Jansky/beam. We shall write this as  $I_\nu^{\text{jpb}}$ . The conversion is

$$I_\nu = 10^{-23} \frac{\pi(\text{au/pc})^2 b_{\text{as}}^2}{4 \ln(2)} \frac{1}{b_{\text{as}}^2} I_\nu^{\text{jpb}} = 3.755 \times 10^{-13} \frac{1}{b_{\text{as}}^2} I_\nu^{\text{jpb}} \quad (\text{A.1})$$

where

$$b_{\text{as}} = \sqrt{b_{\text{as}}^{\parallel} b_{\text{as}}^{\perp}} \quad (\text{A.2})$$

is the position-angle-averaged beam full-width-at-half-maximum in units of arcseconds. Alternatively it can be expressed as brightness temperature  $T_\nu^{\text{b}}$  in Kelvin by solving the equation

$$I_\nu = B_\nu(T_\nu^{\text{b}}) \quad (\text{A.3})$$

where  $B_\nu(T) = 2h\nu^3 c^{-2} / (\exp(h\nu/k_B T) - 1)$  is the Planck function with  $h$  Planck's constant,  $k_B$  Boltzmann's constant and  $c$  the light speed. The relation between brightness temperature and intensity is non-linear, which is inconvenient. As an alternative to the brightness temperature (henceforth called “full brightness temperature”) we therefore use the *linear* brightness temperature  $I_\nu^{\text{lb}}$ , also expressed in Kelvin, defined as

$$I_\nu^{\text{lb}} = \frac{c^2}{2\nu^2 k_B} I_\nu = 3.255 \times 10^{36} \frac{1}{\nu^2} I_\nu \quad (\text{A.4})$$

The linear brightness temperature is thus a linear representation of the intensity, which is why we use the symbol  $I_\nu^{\text{lb}}$  instead of  $T_\nu^{\text{lb}}$ . The full brightness temperature and the linear brightness temperature become equal in the Rayleigh-Jeans regime. However, at the wavelength we are working in (ALMA band 6 at  $\lambda \simeq 0.13 \text{ cm}$ ) and the temperatures we are dealing with (several Kelvins to tens of Kelvins) we are not in the Rayleigh-Jeans regime anymore, so the distinction between linear and non-linear brightness temperature becomes important.

The conversion between the full brightness temperature  $T_\nu^{\text{b}}$  and the linear brightness temperature  $I_\nu^{\text{lb}}$  is given by

$$\frac{h\nu}{k_B T_\nu^{\text{b}}} = \ln \left( 1 + \frac{h\nu}{k_B I_\nu^{\text{lb}}} \right) \quad (\text{A.5})$$

where in our case, with  $\lambda = 0.13 \text{ cm}$ , we have  $h\nu/k_B = 11 \text{ K}$ .

The Planck function in units of Kelvin, to be used in conjunction with the brightness, is then

$$B_\nu^{\text{lb}}(T) = \frac{h\nu}{k_B} \frac{1}{e^{h\nu/k_B T} - 1} \quad (\text{A.6})$$

so that at high optical depth the brightness saturates to  $I_\nu^{\text{lb}} = B_\nu^{\text{lb}}(T)$ . Throughout this paper we express the intensity as  $I_\nu^{\text{lb}}$ .

## Appendix B: Gauss fitting procedure

In this paper we study each dust ring individually, and try to understand it in terms of the trapping of dust in a pressure trap. In Appendix E we find that for a Gaussian pressure bump the solution to the radial dust mixing and drift problem is, to first approximation, also a Gaussian, albeit a narrower one. Fitting the dust trapping model to the data can therefore be done in two stages: first fitting a Gaussian radial profile to the observed rings, then interpreting these Gaussian fits through the dust trapping model. In this Appendix we detail the procedure we used to fit the radial intensity profiles of the rings with Gaussian profiles.

Source	Ring	$A$	$r_0$	$\sigma$
AS 209	1	$3.637^{+0.048}_{-0.047}$	$74.129^{+0.063}_{-0.066}$	$3.885^{+0.098}_{-0.090}$
AS 209	2	$2.949^{+0.030}_{-0.031}$	$120.309^{+0.065}_{-0.068}$	$4.651^{+0.115}_{-0.111}$
Elias 24	1	$5.214^{+0.066}_{-0.068}$	$76.851^{+0.088}_{-0.092}$	$5.104^{+0.186}_{-0.172}$
HD 163296	1	$8.475^{+0.056}_{-0.056}$	$67.403^{+0.057}_{-0.055}$	$7.370^{+0.098}_{-0.098}$
HD 163296	2	$4.918^{+0.027}_{-0.026}$	$99.862^{+0.059}_{-0.061}$	$5.741^{+0.119}_{-0.116}$
GW Lup	1	$1.467^{+0.055}_{-0.052}$	$85.178^{+0.316}_{-0.259}$	$4.882^{+0.530}_{-0.402}$
HD 143006	1	$3.202^{+0.082}_{-0.084}$	$41.080^{+0.190}_{-0.169}$	$5.133^{+0.373}_{-0.320}$
HD 143006	2	$2.473^{+0.044}_{-0.043}$	$64.831^{+0.230}_{-0.248}$	$8.029^{+0.593}_{-0.501}$

**Table B.1.** The Gaussian fit values with their error estimates from the MCMC procedure described in Appendix B.

The radial intensity profiles (expressed as linear brightness temperature) were extracted from the images using a procedure similar to that described by Huang et al. (2018). This procedure involves the fitting of an ellipse to describe the inclined ring shape, the deprojection into a ring, and the averaging of the intensity along the ring. This averaging procedure enhances the signal-to-noise ratio considerably, by a factor  $\sqrt{N}$ , where  $N$  is the number of beams that fit along the ring. We estimate the intrinsic noise simply by computing the standard deviation along the ring. The resulting averaged radial intensity profile  $I_\nu^{\text{lb}}(r)$  thus obtains also an error estimate  $\varepsilon(r)$ , which is typically of the order of  $\sim 1\%$  of the peak intensity.

The rings display themselves as bumps in  $I_\nu^{\text{lb}}(r)$ . We choose by eye a radial domain around the bump where we believe a Gaussian description is justified. The inner and outer radii of this domain are listed in Table 2. By choosing this domain we can select a specific ring to fit, which is not possible when doing the fitting procedure in the uv-plane.

We now fit a Gaussian profile to this bump

$$I_\nu^{\text{lb,gauss}}(r) = A \exp\left(-\frac{(r - r_0)^2}{2\sigma^2}\right) \quad (\text{B.1})$$

We use the code `emcee` (Foreman-Mackey et al. 2013) to perform a Markov Chain Monte Carlo procedure to find the set of parameters  $(A, r_0, \sigma)$  which have the highest likelihood. Given that the radial sampling of  $I_\nu^{\text{lb,gauss}}(r)$  is about  $N \simeq 70$  points per beam, we have to multiply the error estimate of the datapoints by  $\sqrt{N}$  before feeding it into `emcee`, otherwise the MCMC procedure would treat each sampling point as an independent measuring point, which is not the case.

We show the corner plot of the fitting of ring 1 of AS 209 in Fig. B.1. The plots for the other rings are similar, and are provided in the online material. **TODO: PUT OTHER PLOTS IN ONLINE MATERIAL.**

The most likely parameter values and their error estimates are given in Table B.1.

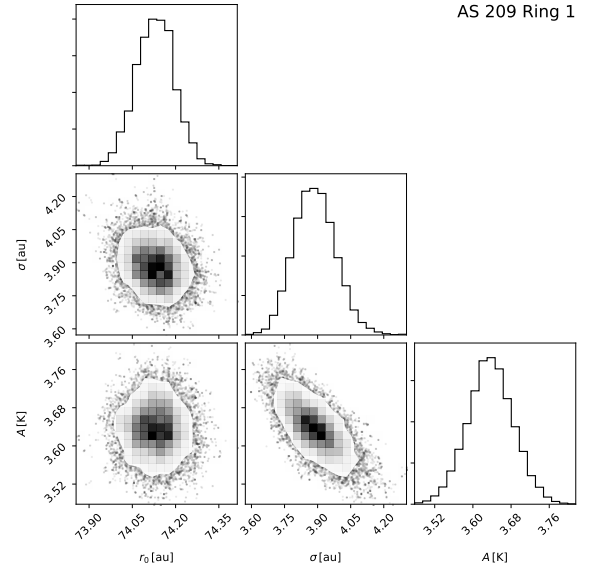


**Fig. B.1.** The correlation plot for the Gauss fitting of ring 1 of AS 209, from the MCMC procedure described in Appendix B.

### Appendix C: Gaussian mimicry: Detectability of mild optical depth effects

As was discussed in Section 5.2, the saturation effect of radiative transfer leads to Gaussian radial profiles of the rings to be flattened at the peak by the  $1 - e^{-\tau_\nu}$  self-absorption effect. The resulting flat-topped profile deviates from the optically thin approximation (which is proportional to  $\tau_\nu$ ) by a factor  $(1 - e^{-\tau_\nu})/\tau_\nu$ . This leads, for  $\tau_\nu^{\text{peak}} \gtrsim 0.6$ , to a substantial reduction near the peak. However, for  $\tau_\nu^{\text{peak}} \lesssim 1$ , the *shape* of the profile stays remarkably close to a Gaussian profile, albeit one that is wider and weaker than the underlying  $\tau_\nu(r)$ . If the differences lie within the errorbars of the observations, there is no way to tell the difference.

This ‘mimicry’ (a non-Gaussian function posing as a Gaussian one) makes it hard to exclude, from looking at the shape of the profile (it being not ‘flat-topped’), that optical depth effects play a role. Given that much of our analysis of the rings in terms of dust trapping relies on the optically thin approximation (“what you see is what is there”), it is important to quantify this. This is the topic of this appendix.

We do the following experiment: We start from a simple Gaussian function  $g(x)$  given by

$$g(x) = \exp\left(-\frac{1}{2}x^2\right) \quad (\text{C.1})$$

where  $x = (r - r_0)/w_d$ . From this we generate the optical depth profile

$$\tau_\nu(x) = \tau_\nu^{\text{peak}} g(x) \quad (\text{C.2})$$

for a given value of  $\tau_\nu^{\text{peak}}$ . We then compute the function

$$f(x) \equiv \frac{I_\nu^{\text{lb}}(x)}{B_\nu^{\text{lb}}(T_d)} = 1 - e^{-\tau_\nu(x)} \quad (\text{C.3})$$



The results, for different values of  $\tau_\nu^{\text{peak}}$ , are shown in the left panel of Fig. C.1. As one can see, the differences between  $\tau_\nu(x)$  and  $f(x)$  become quite substantial for  $\tau_\nu^{\text{peak}} \simeq 0.7$ .

For both  $\tau_\nu(x)$  and  $f(x)$  we now compute the beam-convolved versions:

$$\tau_\nu^{\text{conv}}(x) = \frac{1}{\sqrt{2\pi}\sigma_{\text{beam}}} \int_{-\infty}^{+\infty} \tau_\nu(x') \exp\left(-\frac{(x-x')^2}{2\sigma_{\text{beam}}^2}\right) dx' \quad (\text{C.4})$$

and likewise for  $f(x)$ , where  $\sigma_{\text{beam}}$  is the standard-deviation beam width in  $x$ -units. In this experiment the width of the underlying Gaussian ‘dust distribution’ (Eq. C.1) stays always fixed at  $\sigma_{\text{gauss}} = 1$ , and the beam size is expressed in relation to that. For the example of a beam that is half the width of the Gaussian profile of  $\tau_\nu(x)$  (corresponding roughly to ring 1 of AS 209, for instance) the results are shown in the middle panel of Fig. C.1. This panel shows that the beam convolution changes the results only by a little, at least for beams smaller than, or equal to, the original width of the dust distribution. Given that all the rings of this paper appear to be spatially resolved, we do not consider larger beams here.

Now we try to find the best-fit Gaussian profile for  $f(x)$ . We do that by constructing an alternative Gaussian function  $\tilde{g}(x)$

$$\tilde{g}(x) = \tilde{a} \exp\left(-\frac{x^2}{2\tilde{\sigma}^2}\right) \quad (\text{C.5})$$

where, in contrast to the original  $g(x)$  of Eq. (C.1), the  $\tilde{a}$  and  $\tilde{\sigma}$  are free parameters to fit. We subsequently obtain  $\tilde{\tau}_\nu(x)$  and  $\tilde{\tau}_\nu^{\text{conv}}(x)$  by the same procedure as above, then then use a minimization procedure to find the values of  $\tilde{a}$  and  $\tilde{\sigma}$  for which the difference to the function  $f^{\text{conv}}(x)$  is minimal. We then plot the resulting  $\tilde{\tau}_\nu^{\text{conv}}(x)$  as dashed lines in the right panel of Fig. C.1. One can see that even for the case of  $\tau_\nu^{\text{peak}} = 3.0$  the Gaussian fit mimicks the real curve remarkably (or perhaps disturbingly) well. Given the high signal to noise we have in our azimuthally-averaged radial profiles (see Fig. 3), we can nevertheless exclude the case  $\tau_\nu^{\text{peak}} = 3.0$ . But it is much harder to exclude the case  $\tau_\nu^{\text{peak}} = 1.2$ , and impossible to exclude the case  $\tau_\nu^{\text{peak}} = 0.7$ .

To quantify this a bit better, we have run the above models for a 2-D grid of parameters  $(\sigma_{\text{beam}}, \tau_\nu^{\text{peak}})$ , and computed, for each pair of parameters, the following quantities:

$$\mathcal{W} = \tilde{\sigma} \quad (\text{C.6})$$

$$\mathcal{M} = \tilde{a} \quad (\text{C.7})$$

$$\mathcal{T} = f^{\text{conv}}(x=0) \quad (\text{C.8})$$

$$\mathcal{F} = \tilde{\tau}_\nu^{\text{conv}}(0)/f^{\text{conv}}(x=0) \quad (\text{C.9})$$

They are plotted in Fig. C.2. The  $\mathcal{W}$  parameter tells us how much the mimicry will lead to an overestimation of the true width of the dust distribution. The  $\mathcal{M}$  parameter tells us how much we would underestimate the dust mass by this effect. The  $\mathcal{T}$  parameter tells us the degree

to which we underestimate the true linear brightness temperature  $B_\nu^{\text{lb}}(T_d)$  (and by inference, the true dust temperature  $T_d$ ) if we would interpret the observed linear brightness temperature as if it were optically thick (i.e. by setting  $B_\nu^{\text{lb}}(T_d) = I_\nu^{\text{lb,obs}}$ ). For the case of no convolution this becomes  $\mathcal{T} = 1 - e^{-\tau_\nu^{\text{peak}}}$ . Finally the  $\mathcal{F}$  parameter gives the ratio of the mimicking Gauss function to the real  $f^{\text{conv}}$  function, at  $x = 0$ , as a representation of ‘how bad is the mimicking’. The closer  $\mathcal{F}$  is to 1, the better is the mimicking, meaning the more difficult it is to distinguish the real from the mimicked curve. If  $\mathcal{F} - 1$  is less than the relative error of the observations at the peak of the curve, then they are indistinguishable.

These results show that up to  $\tau_\nu^{\text{peak}} \lesssim 1$  the differences between the best-fit Gauss and the real curve are at most  $\sim 1 \dots 2$  %, depending on the beam size. The beam size has most influence on  $\mathcal{F}$ , but less on the other parameters. That is because many of the effects of beam smearing are cancelled out because we know the beam size and can deconvolve. But the beam smearing does make a non-Gaussian profile more Gaussian-shaped, hence the stronger effect on  $\mathcal{F}$ .

Although the mimicry effect is bad news for the interpretation of the observed radial ring profiles, the upper-left panel of Fig. C.2 shows that the effect on the derived width of the dust ring remains modest. The fact that the widths of the rings in our sample all seem to be spatially resolved by at least 2 beam widths can therefore not be due to an unresolved dust ring being broadened by the optical depth effect. To broaden by a factor of 2 (i.e.  $\mathcal{W} = 2$ ) you would need an optical depth so large that the mimicry will clearly fail, i.e. we would easily recognize the deviations from a Gaussian shape.

#### Appendix D: Thermal emission from a thin dust layer with scattering

So far we have assumed that only the absorption opacity  $\kappa_\nu^{\text{abs}}$ , not the scattering opacity, matters. For optically thin dust layers this is indeed appropriate. But we have seen in Sections 4 and 5 that the optical depth are not that low. Furthermore, the CO line extinction data of HD 163296 discussed by Isella et al. (2018) suggest that the dust layer has an extinction optical depth close to unity. Even if the absorption optical depth is substantially below 1, the total extinction (absorption + scattering) can easily exceed unity, if the grains are of similar size to the wavelength. For  $a \simeq \lambda/2\pi = 0.13/2\pi = 0.02$  cm the albedo of the grain can, in fact, be as high as 0.8 **CHECK**.

The inclusion of scattering complicates the radiative transfer equation enormously. Strictly speaking a full radiative transfer calculation, for instance with a Monte Carlo code, is necessary. However, in the spirit of this paper we wish to find a simple approximation to handle this without resorting to numerical simulation.

We will outline here a simple two-stream radiative transfer approach to the problem. We will assume that the dust seen in the ALMA observations is located in a

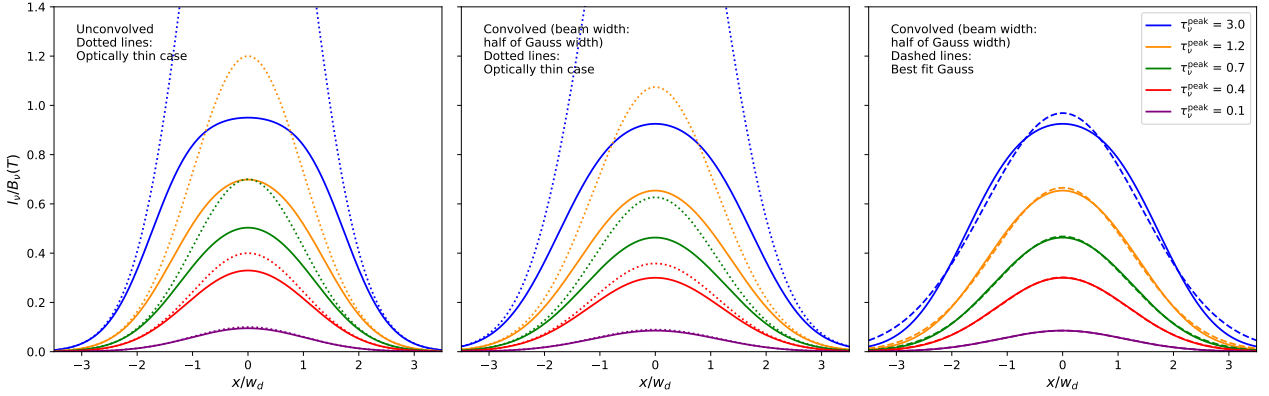


**Fig. C.1.** Demonstration of the Gaussian ‘mimicry’ effect discussed in Appendix C. Left panel: Profiles before beam-convolution. Solid curves show the radiative transfer result  $f(x) = 1 - e^{-\tau_\nu(x)}$ , dotted curves show the underlying  $\tau_\nu(x)$ . Middle panel is the same, but convolved with a beam that is half the width of the Gaussian profile of  $\tau_\nu(x)$ . Right panel: Solid lines are the same as for the middle panel, but the dashed lines are the best fit Gaussian curves (also convolved with the beam).

geometrically thin layer at the midplane, so we can use the 1-D slab geometry approach. We will assume that the scattering is isotropic. This may be a bad approximation, especially for  $2\pi a \gg \lambda$ . To reduce the impact of this approximation we replace the scattering opacity  $\kappa_\nu^{\text{scat}}$  with

$$\kappa_\nu^{\text{scat,eff}} = (1 - g_\nu) \kappa_\nu^{\text{scat}} \quad (\text{D.1})$$

where  $g_\nu$  is the usual forward-scattering parameter (the expectation value of  $\cos \theta$ , where  $\theta$  is the scattering angle). According to Ishimaru (1978), this approximation works well in optically thick media.

We will now follow the two-stream / moment method approach from Rybicki & Lightman (1986) to derive the solution to the emission/absorption/scattering problem in this slab. The slab is put between  $z = -\frac{1}{2}\Delta z$  and  $z = +\frac{1}{2}\Delta z$  and we assume a constant density of dust between these two boundaries. The mean intensity  $J_\nu(z)$  of the radiation field then obeys the equation

$$\frac{1}{3} \frac{d^2 J_\nu(\tau)}{d\tau_\nu^2} = \epsilon_\nu (J_\nu - B_\nu(T_d)) \quad (\text{D.2})$$

where

$$\tau_\nu = \rho_d (\kappa_\nu^{\text{abs}} + \kappa_\nu^{\text{scat,eff}}) z \equiv \rho_d \kappa_\nu^{\text{tot}} z \quad (\text{D.3})$$

with  $\rho_d$  being the dust density, and

$$\epsilon_\nu = \frac{\kappa_\nu^{\text{abs}}}{\kappa_\nu^{\text{abs}} + \kappa_\nu^{\text{scat,eff}}} \quad (\text{D.4})$$

The boundary conditions at  $z = \pm \frac{1}{2}\Delta z$  are

$$\frac{dJ_\nu}{d\tau_\nu} = \mp \sqrt{3} J_\nu \quad (\text{D.5})$$

This leads to the following solution:

$$\frac{J_\nu(\tau_\nu)}{B_\nu(T_d)} = 1 - b \left( e^{-\sqrt{3\epsilon_\nu}(\frac{1}{2}\Delta\tau - \tau_\nu)} + e^{-\sqrt{3\epsilon_\nu}(\frac{1}{2}\Delta\tau + \tau_\nu)} \right) \quad (\text{D.6})$$

where  $\Delta\tau = \rho_d \kappa_\nu^{\text{tot}} \Delta z$  and  $b$  is

$$b = \left[ (1 - \sqrt{\epsilon_\nu}) e^{-\sqrt{3\epsilon_\nu}\Delta\tau} + 1 + \sqrt{\epsilon_\nu} \right]^{-1} \quad (\text{D.7})$$

Given this solution for the mean intensity  $J_\nu(\tau_\nu)$  we can now numerically integrate the formal transfer equation along a single line of sight passing through the slab at an angle  $\theta$ :

$$\mu \frac{dI_\nu(\tau_\nu)}{d\tau_\nu} = \epsilon_\nu B_\nu(T_d) + (1 - \epsilon_\nu) J_\nu(\tau_\nu) - I_\nu(\tau_\nu) \quad (\text{D.8})$$

where  $\mu = \cos \theta$ . We start at  $\tau_\nu = -\frac{1}{2}\Delta\tau$  with  $I_\nu = 0$  and integrate to  $\tau_\nu = +\frac{1}{2}\Delta\tau$ . The resulting  $I_\nu^{\text{out}} = I_\nu(\frac{1}{2}\Delta\tau)$  is the intensity that is observed by the telescope. An approximation for  $I_\nu^{\text{out}}$  which works well to within a few percent is the following modified version of the Eddington-Barbier approximation:

$$I_\nu^{\text{out}} \simeq \left( 1 - e^{-\Delta\tau/\mu} \right) S_\nu \left( (\frac{1}{2}\Delta\tau - \tau_\nu)/\mu = 2/3 \right) \quad (\text{D.9})$$

where

$$S_\nu(\tau_\nu) = \epsilon_\nu B_\nu(T_d) + (1 - \epsilon_\nu) J_\nu(\tau_\nu) \quad (\text{D.10})$$

is the source function. The results are shown in Fig. D.1.

For small optical depths ( $\Delta\tau \ll 1$ ) the role of scattering vanishes, and the solution approaches:  $I_\nu^{\text{out}} \rightarrow \epsilon_\nu \Delta\tau B_\nu(T_d)$ . This is the same limiting solution as when  $\kappa_\nu^{\text{scat}}$  is set to zero but  $\kappa_\nu^{\text{abs}}$  is kept the same. For high optical depth the outgoing intensity does not saturate to the Planck function, but a bit below, if the albedo is non-zero. This is the well-known effect that scattering makes objects appear cooler than they really are.

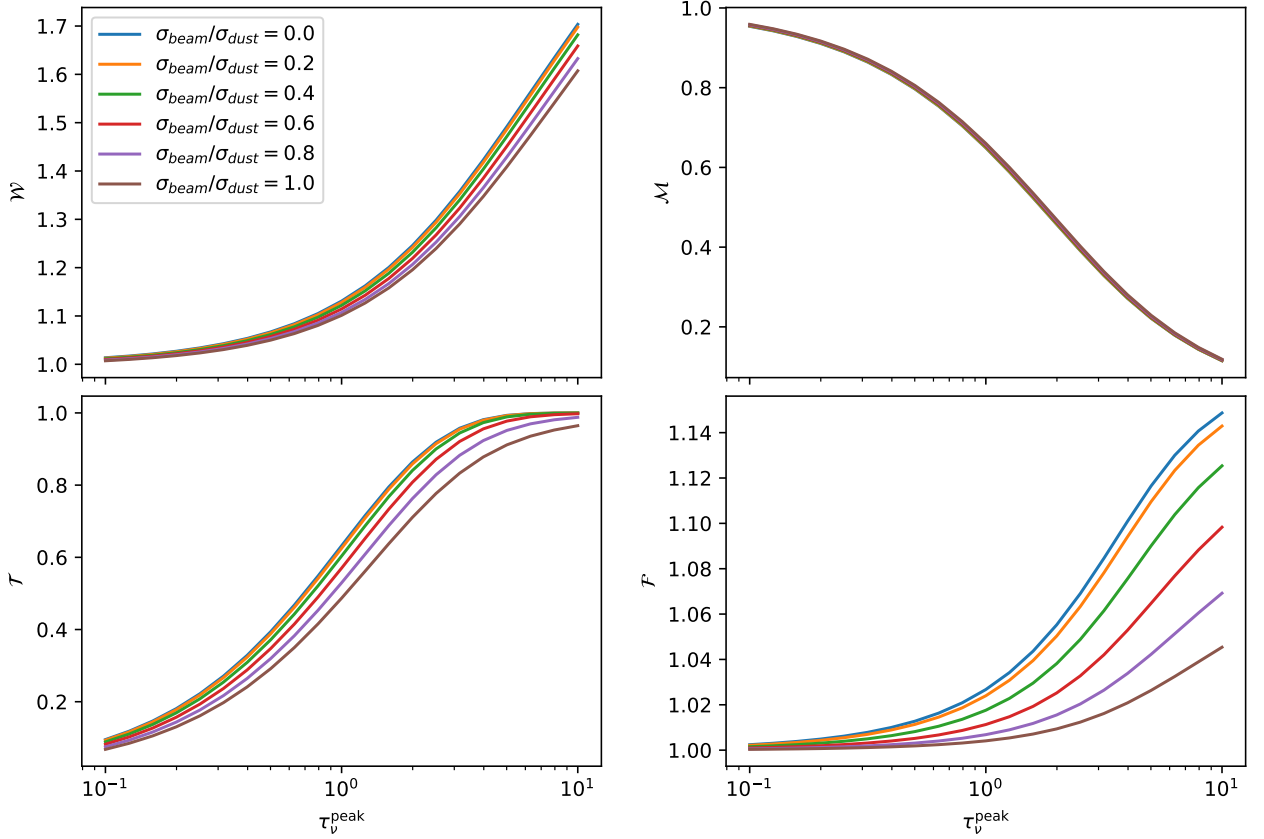


**Fig. C.2.** A quantitative analysis of the mimicry effect of Appendix C, scanning the two parameters of the model: ( $\sigma_{\text{beam}}, \tau_{\nu}^{\text{peak}}$ ). The four panels show the four derived parameters explained in the text. Upper left shows the degree of overestimation of the width, upper right the degree of underestimation of the dust mass, bottom left the underestimation of the temperature, bottom right an estimate of the deviation of the Gauss fit to the real curve (the closer to unity, the better the mimicry, and therefore the worse the interpretation of the observations in terms of an optically thin model).

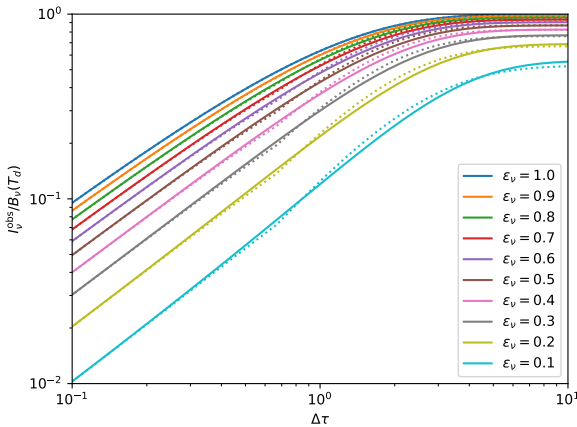


**Fig. D.1.** The intensity  $I_{\nu}$ , in units of the Planck function, emerging from a slab seen face on, with total optical depth  $\Delta\tau$ , a constant temperature, and an albedo of  $\eta_{\nu} = 1 - \epsilon_{\nu}$ . See Appendix D for details. The solid lines are the results of numerical integration of Eq. (D.8). The dotted lines are the result of the modified Eddington-Barbier approximation (Eq. D.9).

## Appendix E: Steady-state dust distribution in a ringlike trap

### E.1. Analytic approximate solution of dust trapping

Let us consider a narrow gas ring around the star at radius  $r_0$  with a midplane pressure given by

$$p(r) = p_0 \exp\left(-\frac{(r - r_0)^2}{2w^2}\right) \quad (\text{E.1})$$

where  $w \ll r_0$  is the parameter setting the width of this gaussian gas ring. We assume that the gas is turbulent with turbulent diffusion coefficient  $D$ . Dust grains get trapped in this ring, and the dust will acquire a radial density profile that is in equilibrium between the radial dust drift pointing toward the peak of the gas pressure and radial turbulent diffusion pointing away from that position. The radial dust drift velocity is (see e.g. Birnstiel et al. 2010):

$$v_{\text{dr}} = \frac{\text{St}}{1 + \text{St}^2} \left( \frac{d \ln p}{d \ln r} \right) \frac{c_s^2}{\Omega_K r} \quad (\text{E.2})$$

where  $c_s$  is the isothermal sound speed and the Stokes number  $St$  is defined as

$$St = \Omega_K t_{\text{stop}} \quad (\text{E.3})$$

where  $t_{\text{stop}}$  is the stopping time of the grains. The diffusion coefficient for the dust is (Youdin & Lithwick 2007):

$$D_d = \frac{D}{1 + St^2} \quad (\text{E.4})$$

We take  $D$  to be equal to the turbulent viscosity  $\nu$  divided by the Schmidt number  $Sc$ , which we usually set to  $Sc = 1$ . We use the usual  $\alpha$ -prescription for the turbulence:

$$D = \frac{\nu}{Sc} = \alpha_{\text{turb}} \frac{c_s^2}{Sc \Omega_K} \quad (\text{E.5})$$

If  $D$  is sufficiently small, the dust will get concentrated into a ring with width  $w_d$  that is substantially smaller than the width of the gas ring  $w$ . In the following, we will ignore any terms arising from the curvature of the coordinates. The steady-state radial diff-mixing equation for the dust then becomes, in its approximate form:

$$\frac{d}{dr} \left( \Sigma_d v_{\text{dr}} - D_d \frac{d\Sigma_d}{dr} \right) = 0 \quad (\text{E.6})$$

Integrating this equation once, with integration constant zero (which amounts to a zero net radial flux), yields

$$\Sigma_d v_{\text{dr}} = D_d \frac{d\Sigma_d}{dr} \quad (\text{E.7})$$

From Eqs.(E.2,E.1) we can express  $v_{\text{dr}}$  as

$$v_{\text{dr}} = - \left( \frac{c_s^2}{w^2 \Omega_K (St + St^{-1})} \right) (r - r_0) \quad (\text{E.8})$$

With this expression we can solve Eq. (E.7) for  $\Sigma_d$ , leading to the following simple analytic solution to the dust trapping problem:

$$\Sigma_d(r) = \Sigma_{d0} \exp \left( - \frac{(r - r_0)^2}{2w_d^2} \right) \quad (\text{E.9})$$

with

$$w_d = w \sqrt{\frac{\Omega_K D_d (St + St^{-1})}{c_s^2}} = w \sqrt{\frac{\alpha_{\text{turb}}}{Sc St}} \quad (\text{E.10})$$

The normalization constant  $\Sigma_{d0}$  can be approximately expressed in terms of the total dust mass trapped in the pressure bump:

$$M_d = 2\pi \int_0^\infty \Sigma_d(r) r dr \simeq 2\pi r_0 \int_0^\infty \Sigma_d(r) dr \quad (\text{E.11})$$

which leads to

$$\Sigma_{d0} \simeq \frac{M_d}{(2\pi)^{3/2} r_0 w_d} \quad (\text{E.12})$$

The approximation is best for narrow dust rings.

Note that this analytic solution is only valid as long as  $\alpha_{\text{turb}} \ll Sc St$ , or in other words as long as  $w_d$  is substantially smaller than  $w$ . This solution is, in fact, the radial version of the vertical settling-mixing equilibrium solutions of Dubrulle et al. (1995).

Unfortunately, the condition that  $\alpha_{\text{turb}} \ll Sc St$  (and equivalently  $w_d \ll w$ ) is easily broken for small grains and/or non-weak turbulence. This is similar to the case for vertical settling and mixing: Small grains tend not to settle below a few pressure scale heights. They settle down to some critical  $z_{\text{settle}}$ , below which they are well mixed with the gas, and above which they are strongly depleted (Dullemond & Dominik 2004). Fromang & Nelson (2009) give an analytic solution to the settling-mixing problem (their Eq. 19) that reproduces the solutions of Dubrulle et al. (1995) for  $\alpha_{\text{turb}} \ll Sc St$ , but at the same time remains valid also for  $\alpha_{\text{turb}} \gtrsim Sc St$ , as long as  $\alpha_{\text{turb}}$ ,  $Sc$  and  $St$  remain constant with height above the midplane.

Given the similarity between the radial dust trapping problem and the vertical settling problem, one can show that the radial version of the solution of Fromang & Nelson (2009) reads:

$$\Sigma_d(r) = \Sigma_{d0} \exp \left[ - \frac{Sc St}{\alpha_{\text{turb}}} \left( \exp \left( \frac{\Delta r^2}{2w^2} \right) - 1 \right) - \frac{\Delta r^2}{2w^2} \right] \quad (\text{E.13})$$

where we defined  $\Delta r$  as

$$\Delta r \equiv (r - r_0) \quad (\text{E.14})$$

The solution Eq. (E.13) is valid for any value of  $\alpha_{\text{turb}}/Sc St$ , as long as  $\alpha_{\text{turb}}$ ,  $Sc$  and  $St$  remain constant along the radial width of the dust trap, and as long as  $w \ll r_0$ , to prevent geometric terms from the cylindrical coordinates from dominating. One can easily verify that Eq. (E.13) reproduces the simpler Gaussian solution Eq. (E.9) for  $\Delta r \ll w$ . One can also verify that for  $\alpha_{\text{turb}} \gg Sc St$  the shape of  $\Sigma_d(r)$  follows the shape of the gas pressure profile  $p(r)$  (Eq. E.1).

The solution Eq. (E.13), like its simplified version Eq. (E.9), assumes that the dust is always near the midplane of the disk, so that one can ignore the vertical extent, and thereby ignore any variations in  $St$ . In other words, we assume that the vertical scale height of the dust layer  $h_d$  is much less than the gas pressure scale height  $h_p$ . As it turns out, this condition  $h_d \ll h_p$  is satisfied if  $\alpha_{\text{turb}} \ll Sc St$ , which is the same condition that leads to  $w_d \ll w$  (at least for  $St \ll 1$ , which is what we assume). In fact, the radial dust ring width compared to the gas ring width is the same as the vertical dust layer thickness compared to the gas disk thickness:

$$\frac{w_d}{w} = \frac{h_d}{h_p} \quad (\text{E.15})$$

In other words: the dust behaves radially the same way as vertically. The vertical dust settling can be regarded as dust trapping in vertical direction, or the radial dust trapping can be seen as radial settling of dust toward the pressure peak.

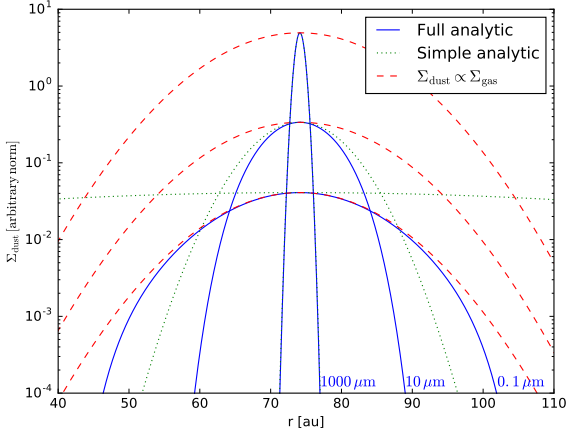


**Fig. E.1.** The analytic solution shown for three different grain sizes: small ( $0.1 \mu\text{m}$ ), middle middle ( $10 \mu\text{m}$ ) and large ( $1000 \mu\text{m}$ ). The normalizations of the three curves are arbitrary, optimized for clarity. The solid (blue) curves show the full analytic solution (Eq. E.13). The dotted (green) curves show the simplified analytic solution (Eq. E.9). The dashed (red) curves show the dust profile *if* the dust-to-gas ratio would be constant, which shows the shape of the gas pressure bump. The absence of the green dotted curve for the case of  $1000 \mu\text{m}$  grains (the narrowest peak) is because for these large grains the simple analytic solution nearly perfectly overlaps with the full analytic solution. The parameters are chosen for AS 209, ring 1, with  $M_* = 0.912 M_\odot$ ,  $T_{\text{gas}} = 12.9 \text{ K}$ . The gas surface density is taken to be  $5 \text{ g/cm}^2$  at the position of the ring, the turbulence parameter was set to  $\alpha_{\text{turb}} = 2 \times 10^{-4}$ , the dust material density was chosen to be  $2 \text{ g/cm}^3$  consistent with slightly porous silicate dust aggregates. **[CHECK IF THIS IS CONSISTENT WITH THE OPACITY ESTIMATES, IN PARTICULAR THE RICCI OPACITY.]** The standard-deviation width of the gas pressure bump was set to  $w = 9.7 \text{ au}$  which equals two times the gas pressure scale height.

This also means that whenever the simplified Gaussian analytic solution (Eq. E.9) ceases to be valid, so does the simplified vertical Gaussian solution of Dubrulle et al. (1995). Or in other words, whenever the more sophisticated analytic solution Eq. (E.13) should be used instead of the simplified version, the assumption that the dust is settled near the midplane ceases to hold. Strictly speaking this invalidates Eq. (E.13), since this was derived under the assumption that the dust is all located near the midplane. But given that most of the dust mass is still close to the midplane, even for  $\alpha_{\text{turb}} \gtrsim \text{Sc St}$ , we are confident that Eq. (E.13) still remains approximately valid.

The typical shapes of the analytic dust surface density profiles is shown in Fig. E.1 for three different grain sizes from small to large. For the largest grains, which are the most strongly trapped near the pressure peak, and hence have the narrowest peak in Fig. E.1, the full an-

alytic solution (Eq. E.13) nearly perfectly overlaps with the simplified (Gaussian) analytic solution (Eq. E.9). For large grains the simplified analytic solution is therefore sufficiently accurate. But in this parameter regime the dust rings are much narrower than the gas pressure bump ( $w_d \ll w$ ).

For the tiny grains, which are well coupled to the gas, and hence have the widest peak in Fig. E.1, the dust trapping is very inefficient. Between 60 and 90 au the dust surface density follows nearly perfectly the shape of the gas bump, i.e. keeping the dust-to-gas ratio nearly constant. Only for  $r \lesssim 60 \text{ au}$  and  $r \gtrsim 90 \text{ au}$  the full solution drops below a constant dust-to-gas ratio. To good approximation one can thus say that a dust ring made up of these tiny grains has a width that equals the width of the gas pressure bump. Note that in this regime the simplified analytic model (Eq. E.9) fails miserably, as can be seen by the nearly horizontal green dotted curve in Fig. E.1.

The intermediate size grains, corresponding to the intermediate curve (marked with  $100 \mu\text{m}$ ) in Fig. E.1, have a behavior between the above two extremes. The simplified analytic solution is a bit wider than the more accurate solution. The shape of the more accurate solution deviates from Gaussian. However, the deviation from Gaussian shape of the model is opposite to the deviation from Gaussian shape in the observations (Fig. 3). The observed data exceed the best-fit Gaussian in the flanks, while the model drops below the best-fit Gaussian in the flanks.

Whether this deviation from Gaussian is detectable in the ALMA data is, however, not so clear. For intermediate size grains the non-Gaussian profile can be easily mistaken for a Gaussian profile with a narrower width than both the gas bump and the simple analytic solution.

## E.2. Resulting profiles for a size distribution

**[THIS SECTION NEEDS HEAVY EDITING]**

The analytic model of the dust trapping for a single grain size speaks for itself. But how does it look for a grain size distribution? Since the trapping width  $w_d$  for the different grain sizes is different, we can only impose the grain size distribution for the total (radially integrated) dust mass. We define the size distribution according to the following powerlaw

$$m(a) \frac{dN}{d \ln a} = \frac{dM}{d \ln a} \propto a^q \quad (\text{E.16})$$

where  $a$  is the grain size,  $m(a)$  the corresponding grain mass,  $N$  the cumulative particle number and  $M$  the cumulative dust mass. The parameter  $q$  is the size distribution powerlaw coefficient, and it is  $q = 1/2$  for the usual MRN distribution (this corresponds to  $dN/da \propto a^{-3.5}$ ). We also need to define limits  $a_{\text{min}}$  and  $a_{\text{max}}$ . The size distribution is then normalized such that its integral over  $d \ln(a)$  is the total dust mass  $M$ . The radial surface density solution,

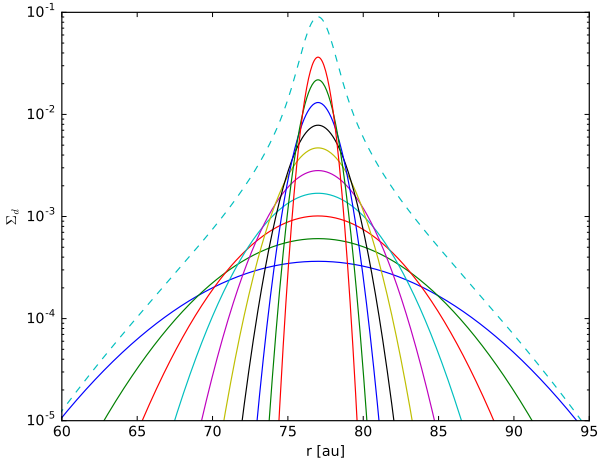


**Fig. E.2.** Results of the analytic dust trapping model for an MRN powerlaw grain size distribution between  $a = 0.01$  cm and  $a = 1$  cm. The gas pressure bump has a FWHM of 70 au and a peak at  $r = 77$  au. Shown here are the surface density profiles for 10 logarithmically binned grain sizes. The curve with the narrowest peak corresponds to a grain size of  $a = 1$  cm, while that with the widest peak (and lowest maximum value) corresponds to a grain size of  $a = 0.01$  cm. The intermediate curves correspond to  $a = 0.0167, 0.0278, 0.0464, 0.0774, 0.1291, 0.2154, 0.3593$  and  $0.5995$  cm respectively. The dashed curve shows the total surface density of the dust, which is, by definition of the bin-integrated surface density, the sum of all 10 curves. For a description of the model setup and model parameters, see Section E.2.

Eq. (E.9), then becomes:

$$\frac{d\Sigma_d(r)}{d \ln a} = \frac{1}{(2\pi)^{3/2} r_0 w_d(a)} \frac{dM}{d \ln a} \exp\left(-\frac{(r - r_0)^2}{2w_d(a)^2}\right) \quad (\text{E.17})$$

In Fig. E.2 we show the radial profiles for an MRN size distribution between  $a_{\min} = 10^{-2}$  cm and  $a_{\max} = 1$  cm and a total dust mass of  $M = 1.3 \times 10^{-5} M_\odot$ . The dust material density is taken to be  $\xi_{\text{dust}} = 2 \text{ g/cm}^3$ . We sample this size distribution with 10 grain sizes, evenly distributed in  $\ln(a)$ . These are the 10 curves in Fig. E.2. These surface densities are defined as being the local grain size distribution integrated over the width of the grain size bin:  $\Sigma_{\text{bin}} = \int_{\text{bin}} (d\Sigma_{\text{dust}}/da) da$ . The stellar mass is  $M_* = 0.9 M_\odot$  and we set  $\text{Sc} = 1$ .

**MUST ALSO SPECIFY GAS DENSITY, TO GET STOKES NUMBERS. MUST SAY (AND CHECK) THAT EPSTEIN REGIME.**

As expected, the largest grains are concentrated the most and the smallest ones the least. The largest grains, however, have the largest peak value of their surface density at the exact location of the gas pressure peak.

When it comes to the contribution to the optical depth, however, the situation looks a bit different. Let us assume a very simple dust opacity law, which roughly mimicks

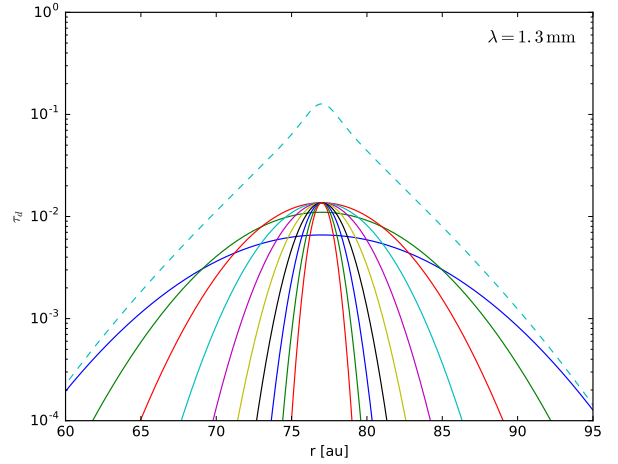


**Fig. E.3.** As Fig. E.2, but now the vertical optical depth at  $\lambda = 1.3$  mm (ALMA band 6) is shown. The opacity model of Ivezić et al. (1997) was used to compute these from the size distribution.

the real behavior of dust opacities: the model of Ivezić et al. (1997), where we take the scattering opacity zero for simplicity. In this simple but illustrative opacity model the cross section of a grain with radius  $a$  is the geometric cross section  $\pi a^2$  for  $2\pi a > \lambda$  (with  $\lambda$  the wavelength), while it is reduced by a factor  $(2\pi a/\lambda)$  for  $2\pi a < \lambda$ . This means that for  $2\pi a > \lambda$  the opacity (that is, the cross section per unit mass) is  $\kappa = 3/4 \xi_{\text{dust}} a$  where  $\xi_{\text{dust}}$  is the material density, here taken to be  $\xi_{\text{dust}} = 2 \text{ g/cm}^3$ . For  $2\pi a < \lambda$  this is reduced by a factor  $(2\pi a/\lambda)$  and thus becomes independent of  $a$ .

It can be seen from Fig. E.3 that at the peak of the trap all grain sizes contribute equally to the optical depth. That is because, with our opacity model, the larger grains (the ones with  $2\pi a > \lambda$ ) have an opacity equal to their geometric cross section per unit dust mass, which goes as  $1/a$ . The smallest grains (the ones with  $a = 0.01$  and  $a = 0.167$ ) have  $2\pi a < \lambda$ , which means that their opacity remains constant with  $a$ . Hence, for these two curves in Fig. E.3 the contribution to the peak optical depth drops below those of the other grains. Of course, with a more realistic opacity model this can change somewhat, but the rough principle remains valid.

More important is to notice that the relative contributions of the grain sizes to the peak optical depth may change if a different grain size distribution is chosen. Here we chose the MRN size distribution ( $q = 1/2$ ), but that was a rather arbitrary choice. Given the complexity of the dust growth processes in protoplanetary disks, it is not at all said that the MRN distribution should be considered a preferred one. The reader may experiment with other values of  $q$  or entirely different grain size distribution shapes altogether.



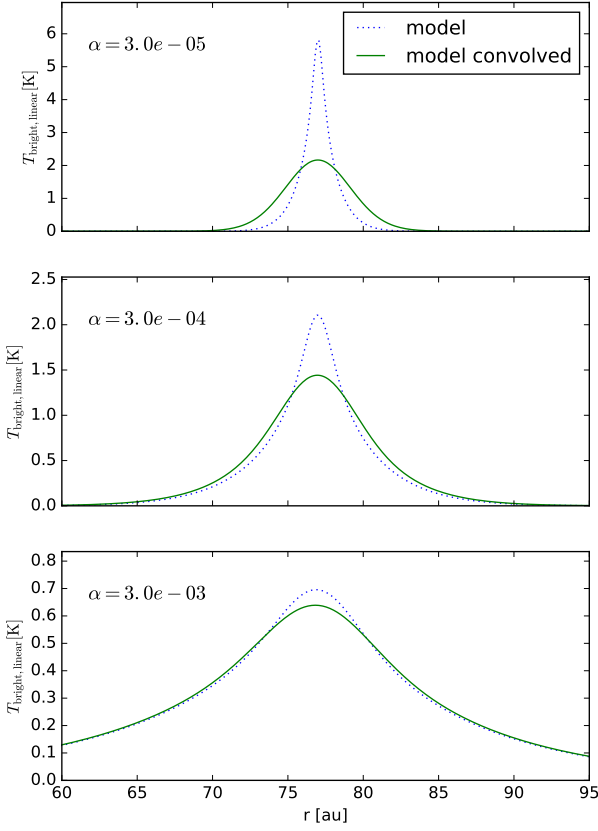


**Fig. E.4.** Results of the analytic dust trapping model for various turbulent strengths, for an MRN powerlaw grain size distribution between  $a = 0.01$  cm and  $a = 1$  cm. The gas pressure bump has a FWHM of 70 au and a peak at  $r = 77$  au. Shown here is the predicted brightness temperature at a wavelength  $\lambda = 1.3$  mm before (dashed) and after (solid) convolution with the ALMA beam, assuming a source distance of  $d = 126$  pc. For a description of the model setup and model parameters, see Section ??.

### E.3. Spectral slope variations across the ring

[TO DO]

### E.4. Leakage and retention time of the dust in the traps

In our analytic model we have assumed that the pressure bump has a perfect Gaussian shape, meaning that the further away one goes from the peak of the trap, the steeper the pressure gradient (and thereby the faster the dust drift) becomes. This leads to perfect trapping: no dust can leak out of the trap. In reality the pressure bump has a finite radial width, and smoothly connects to the global disk structure. There will be a maximum pressure gradient at some distance away from the peak, and beyond that

the pressure gradient declines again. If the width of the trapped dust is much narrower than this distance, virtually no dust will get lost out of the trap. But for small grains and/or strong turbulence, the width of the dust profile may be large enough that at the point of largest pressure gradient there is still a substantial amount of dust. Then the dust will leak out of the trap.

**First make estimates based on current model. Then add the gas radial velocity by accretion.**

### E.5. Stability of gas ring

**Here we must discuss how far into the wings of the gaussian is stable against RWI and other instabilities. Solberg-Hoiland stability criterion. A Gauss may not be very stable in its flanks. This may limit the applicability of the full analytic solution.**

### E.6. Model degeneracies

When trying to infer the effectiveness of dust trapping within the rings with the analytic model of Section E.1, one notices that there are degeneracies in the possible combinations of parameters. Most obvious is the degeneracy between grain size and turbulence: smaller grains and stronger turbulence may yield the same dust trapping width. But also the width of the gas pressure bump can be compensated: a narrower bump but stronger turbulence (or smaller grains) will yield the same ring width.

**[CONTINUE THIS; SOME DEGENERACIES FOLLOW DIRECTLY FROM THE EQUATIONS.]**

#### E.6.1. Could the rings be optically thick at the center?

All rings in our sample show sub-Planckian brightness, at least for the disk temperature assumed in our model. We have calculated the disk midplane temperature using a simple “flaring angle recipe”. If the disks are, however, substantially colder (by up to a factor of 2.5 to 3) then the peak flux of the rings might be consistent with saturated emission, i.e. emission expected from an optically thick disk. So the question is: how sure are we that the rings are sub-Planckian?

To reduce the midplane temperature by a factor of 2 the irradiation flux must be reduced roughly by a factor of  $2^4 = 16$ . Within the flaring angle recipe this would lead to unrealistically low flaring angle. Presently we assumed  $\varphi = 0.02$ , so that it would have to reduce to  $\varphi = 0.0013$ , which is so low that we can no longer trust the flaring angle recipe. However, maybe the outer disk lies in the shadow of the inner disk. To see whether this can reduce the temperature to low enough values, we perform a proper radiative transfer calculation. The results are shown in Appendix (XXXX). It shows that XXXXX.

There is another issue, however. If the emission saturates to the optically thick brightness, i.e. to the Planck

function, then the radial profile of the ring should be flat-topped. This is clearly not what we see in the rings in our sample, with the possible exception of the ring of GW Lup which shows a very slight hint of that. In general, however, it seems that the simple picture of collecting so much dust into the ring that the ring becomes optically thick does not seem to explain the observed radial brightness profiles. On the other hand, optical thickness can also occur on smaller scales, as we will discuss in Section 7.

## **Appendix F: Computing the dust mass trapped in the rings**

**THIS APPENDIX HAS TO BE COMPLETELY REWRITTEN: FOCUS ON OPACITY UNCERTAINTY INSTEAD OF COMPUTATION OF DUST MASS, BECAUSE THE LATTER IS NOW IN THE MAIN TEXT.**